An unsplit Godunov method for ideal MHD via constrained transport

Thomas A. Gardiner [a,*], James M. Stone [a,b]

[a] *Department of Astrophysical Sciences, Princeton University, Peyton Hall, Princeton, NJ 08544, USA*
[b] *Program in Applied and Computational Mathematics, Princeton University, Princeton, NJ 08544, USA*

Abstract

We describe a single step, second-order accurate Godunov scheme for ideal MHD based on combining the piecewise parabolic method (PPM) for performing spatial reconstruction, the corner transport upwind (CTU) method of Colella for multidimensional integration, and the constrained transport (CT) algorithm for preserving the divergence-free constraint on the magnetic field. We adopt the most compact form of CT, which requires the field be represented by area-averages at cell faces. We demonstrate that the fluxes of the area-averaged field used by CT can be made consistent with the fluxes of the volume-averaged field returned by a Riemann solver if they obey certain simple relationships. We use these relationships to derive new algorithms for constructing the CT fluxes at grid cell corners which reduce exactly to the equivalent one-dimensional solver for plane-parallel, grid-aligned flow. We show that the PPM reconstruction algorithm must include multidimensional terms for MHD, and we describe a number of important extensions that must be made to CTU in order for it to be used for MHD with CT. We present the results of a variety of test problems to demonstrate the method is accurate and robust.
© 2004 Elsevier Inc. All rights reserved.

1. Introduction

In recent years a variety of numerical algorithms for multidimensional magnetohydrodynamics (MHD) based on Godunov's method have been developed [3,9,10,16,23,25,28]. There are two important extensions to the basic hydrodynamical algorithm that are required for MHD. The first is an extension of the Riemann solver used to compute the fluxes of each conserved quantity to MHD; the second is a method by which the

divergence-free constraint $\nabla \cdot \mathbf{B} = 0$ is imposed upon the numerically evolved magnetic field. Of the two, the latter has emerged as the more difficult to achieve.

The fact that it is important to ensure the numerically evolved field satisfies the divergence-free constraint was first noted by Brackbill and Barnes [4]. They pointed out that the Lorentz force is not orthogonal to $\mathbf{B}$ if $\nabla \cdot \mathbf{B} \neq 0$, and that this could lead to incorrect dynamics in a well defined test problem. More recently Tóth [32] has shown that in some circumstances it is possible to get the wrong jump conditions across MHD shocks if the constraint is not satisfied (this is also evident in the method of [16]).

Currently, there are three methods by which the divergence-free constraint is applied in Godunov schemes. The first is to use a Hodge projection to clean the magnetic field of any divergence after each time step (e.g. [2,9,32]). The second is to extend the system of conservation laws with an evolutionary equation for the divergence designed to minimize the accumulation of error in any one location. Examples of this approach include the eight-wave scheme [26] and the GLM-MHD scheme [12]. Finally, the third is to design the difference equations for the magnetic field to explicitly conserve magnetic flux, and so preserve the divergence-free constraint. The latter method termed constrained transport (CT) by [15] has proved successfull in other MHD algorithms [6,31] and is the method adopted here.

The most compact CT difference formulae are built upon area-averaged magnetic field components located at the faces of a grid cell, rather than volume-averaged field components located at grid cell centers (CT algorithms built upon cell-centered fields have been developed in [32], however they require averaging over a stencil which is larger than that used to compute the fluxes). The need for a staggered grid is often thought of as a disadvantage of CT. In fact, however, it reflects one of the most attractive properties of CT: the fundamental conserved property of the magnetic field in MHD is the magnetic flux (which is an area- rather than volume-average) and by design, CT conserves the magnetic flux (and therefore it preserves the divergence-free character of the magnetic field) in an integral sense, over the smallest discretization scale, the grid cell size.

We would like to combine CT with a finite volume shock capturing method. It may at first seem inconsistent to build a numerical algorithm which mixes a finite volume approach (which conserves integrals of volume-averaged values) with CT (which conserves integrals of area-averaged magnetic fluxes at grid cell faces). In this paper we show that, provided the fluxes of the volume- and area-averaged fields obey certain simple relationships, the finite-volume and CT approaches can be made consistent (see also [23]). Most importantly, the relationships we derive allow us to develop algorithms for constructing fluxes of the face-centered field (located at grid cell corners in 2D) from the fluxes of the volume-averaged field computed by a Riemann solver (located at grid cell faces). We demonstrate that multidimensional algorithms developed in this way reduce exactly to the equivalent one-dimensional solver for plane-parallel, grid-aligned flow. This is one difference between the methods developed here and previous implementations of CT in Godunov schemes [3,11,28].

We combine the CT algorithms developed in this paper with the piecewise parabolic method (PPM) [8] using Roe's linearization as the MHD Riemann solver [5]. An essential ingredient of PPM is a spatial reconstruction step to compute time-advanced estimates of the conserved variables at grid faces. In this paper we show that for MHD, this reconstruction step must include multidimensional terms in the induction equation (used to reconstruct the transverse components of the field). We argue that dimensionally split MHD algorithms cannot preserve the divergence-free constraint between each one-dimensional update, therefore we adopt the unsplit corner transport upwind (CTU) algorithm of Colella [7] to develop a multidimensional algorithm. However, there are a number of important extensions that must be made to CTU to make it suitable for MHD with CT. These include using a CT update for the magnetic field during the predict step, and inclusion of multidimensional terms along with the transverse flux gradients used to predict multidimensional fluxes. We describe these extensions in detail.

The resulting two-dimensional MHD PPM algorithm uses a single step update, is second order accurate, and is fully conservative. Hence it is ideally suited for use on a statically or adaptively refined mesh. More-

over, the two-dimensional algorithm reduces exactly to the base one-dimensional algorithm for planar, grid-aligned flows. Although this paper will only describe the combination of CT with CTU, there is no reason why the CT algorithm described here could not be combined with other unsplit methods. To simplify the discussion we confine ourselves to a two-dimensional algorithm in this paper.

The paper is organized as follows. In Section 2, we review the finite volume and CT methods in order to demonstrate the relationships between the area- and volume-averaged magnetic fields and their fluxes. In Section 3.3, we use these relationships to derive algorithms for constructing the fluxes of face-centered area-averaged fields needed by CT from the fluxes of cell-centered volume-averaged fields returned by a Riemann solver. We present a single step first-order Godunov method and use it to test different algorithms for constructing the fluxes used in CT. This method forms the first half of the second-order CTU + CT integration algorithm developed in Section 4. In Section 5, we present a variety of tests which demonstrate the linear and nonlinear behavior of the scheme. Finally, in Section 6 we conclude.

2. Constrained transport in finite volume schemes

The equations of ideal magnetohydrodynamics (MHD) can be written in conservative form as

$$\frac{\partial \rho}{\partial t} + \nabla \cdot (\rho \mathbf{v}) = 0, \tag{1}$$

$$\frac{\partial \rho \mathbf{v}}{\partial t} + \nabla \cdot (\rho \mathbf{v} \mathbf{v} - \mathbf{B} \mathbf{B}) + \nabla P^* = 0, \tag{2}$$

$$\frac{\partial \mathbf{B}}{\partial t} + \nabla \cdot (\mathbf{v} \mathbf{B} - \mathbf{B} \mathbf{v}) = 0, \tag{3}$$

$$\frac{\partial E}{\partial t} + \nabla \cdot ((E + P^*) \mathbf{v} - \mathbf{B}(\mathbf{B} \cdot \mathbf{v})) = 0, \tag{4}$$

where ρ is the mass density, $\rho \mathbf{v}$ is the momentum density, $\mathbf{B}$ is the magnetic field, and E is the total energy density. The total pressure $P^* \equiv P + (\mathbf{B} \cdot \mathbf{B})/2$, where P is the gas pressure and the total energy density E is related to the internal energy density ϵ via

$$E \equiv \epsilon + \frac{\rho(\mathbf{v} \cdot \mathbf{v})}{2} + \frac{(\mathbf{B} \cdot \mathbf{B})}{2}. \tag{5}$$

Throughout this paper we will assume an ideal gas equation of state for which $P = (\gamma - 1)\epsilon$, where γ is the ratio of specific heats. Unless otherwise stated, we take $\gamma = 5/3$. None of the main results described in this paper depend directly upon the equation of state. Note also that we have chosen a system of units in which the magnetic permeability $\mu = 1$.

In addition to the evolutionary conservation laws (Eqs. (1)–(4)), the magnetic field must also obey the divergence-free constraint, i.e. $\nabla \cdot \mathbf{B} = 0$. It is of paramount importance that the numerically evolved field satisfy this constraint at all times, otherwise, for example, the system of equations for the conservative variables is inconsistent with the same system written in terms of the primitive variables, i.e. (ρ, $\mathbf{v}$, $\mathbf{B}$, P).

The algorithm described in this paper is built upon finite volume (FV) methods, in which the conserved variables are averaged over grid cell volumes. On the other hand, the CT method is built upon area-averaging of the magnetic field, leading to difference equations for the magnetic flux through the surfaces of grid cells. In the following subsections, we briefly review the FV and CT schemes in order to arrive at consistent relationships between the volume- and area-averaged magnetic field and their associated numerical fluxes.

2.1. Finite volume method

Consider a regular, two-dimensional Cartesian grid with grid cell (i,j) centered at (x_i, y_j) and of size $(\delta x, \delta y)$. The conservative system of equations for ideal MHD can be written in vector form as

$$\frac{\partial q}{\partial t} + \nabla \cdot \mathbf{f} = 0, \tag{6}$$

where

$$q \equiv \begin{pmatrix} \rho \\ \rho v_x \\ \rho v_y \\ \rho v_z \\ B_x \\ B_y \\ B_z \\ E \end{pmatrix} \tag{7}$$

is the vector of conserved variables and

$$f_x \equiv \begin{pmatrix} \rho v_x \\ \rho v_x^2 + P^* - B_x^2 \\ \rho v_x v_y - B_x B_y \\ \rho v_x v_z - B_x B_z \\ 0 \\ v_x B_y - B_x v_y \\ v_x B_z - B_x v_z \\ (E + P^*) v_x - B_x (\mathbf{B} \cdot \mathbf{v}) \end{pmatrix}, \quad f_y \equiv \begin{pmatrix} \rho v_y \\ \rho v_y v_x - B_y B_x \\ \rho v_y^2 + P^* - B_y^2 \\ \rho v_y v_z - B_y B_z \\ v_y B_x - B_y v_x \\ 0 \\ v_y B_z - B_y v_z \\ (E + P^*) v_y - B_y (\mathbf{B} \cdot \mathbf{v}) \end{pmatrix} \tag{8}$$

are the flux vectors. Integrating over the volume of grid cell (i,j) and the time interval $\delta t = t^{n+1} - t^n$ and applying Gauss's theorem we obtain

$$q_{i,j}^{n+1} = q_{i,j}^n + \frac{\delta t}{\delta x} \left(F_{x,i-1/2,j}^{n+1/2} - F_{x,i+1/2,j}^{n+1/2} \right) + \frac{\delta t}{\delta y} \left(F_{y,i,j-1/2}^{n+1/2} - F_{y,i,j+1/2}^{n+1/2} \right) \tag{9}$$

the integral form of the evolution equation. The conserved quantities

$$q_{i,j}^n \equiv \frac{1}{\delta x \delta y} \int_{y_i - \delta y/2}^{y_i + \delta y/2} \int_{x_i - \delta x/2}^{x_i + \delta x/2} q(x, y, t^n) \, dx \, dy \tag{10}$$

are averaged over the grid cell volume and the fluxes

$$F_{x,i\pm1/2,j}^{n+1/2} \equiv \frac{1}{\delta y \delta t} \int_{t^n}^{t^{n+1}} \int_{y_i - \delta y/2}^{y_i + \delta y/2} f_x(x_i \pm \delta x/2, y, t) \, dy \, dt, \tag{11}$$

$$F_{y,i,j\pm1/2}^{n+1/2} \equiv \frac{1}{\delta x \delta t} \int_{t^n}^{t^{n+1}} \int_{x_i - \delta x/2}^{x_i + \delta x/2} f_y(x, y_i \pm \delta y/2, t) \, dx \, dt \tag{12}$$

are averaged over the surface area of a grid cell face and the time interval δt. Typically, one approximates the flux integrals in Eqs. (11) and (12) to some order of accuracy, while maintaining strict conservation by

evolving the conserved quantities through Eq. (9). Note when written in this form, the components of the flux vectors are non-zero for the transverse components of the magnetic field only, meaning that directionally split updates of the volume averaged field based on these fluxes will not generally satisfy the divergence-free constraint between directional sweeps. This suggests directionally split algorithms are inappropriate for MHD.

2.2. Constrained transport method

In the CT method, the integral form of the induction equation is based on area rather then volume averages. Starting from the differential form of the induction equation,

$$\frac{\partial \mathbf{B}}{\partial t} + \nabla \times \mathscr{E} = 0, \tag{13}$$

where the electric field $\mathscr{E} = -\mathbf{v} \times \mathbf{B}$ in ideal MHD, one may integrate over the bounding surface of a grid cell and use Stoke's theorem to obtain

$$B_{x,i\pm1/2,j}^{n+1} = B_{x,i\pm1/2,j}^{n} + \frac{\delta t}{\delta y} \left(\mathscr{E}_{z,i\pm1/2,j-1/2}^{n+1/2} - \mathscr{E}_{z,i\pm1/2,j+1/2}^{n+1/2} \right), \tag{14}$$

$$B_{y,i,j\pm1/2}^{n+1} = B_{y,i,j\pm1/2}^{n} - \frac{\delta t}{\delta x} \left(\mathscr{E}_{z,i-1/2,j\pm1/2}^{n+1/2} - \mathscr{E}_{z,i+1/2,j\pm1/2}^{n+1/2} \right) \tag{15}$$

as the integral form of the evolution equation. The magnetic field components

$$B_{x,i\pm1/2,j}^{n} \equiv \frac{1}{\delta y} \int_{y_i-\delta y/2}^{y_i+\delta y/2} B_x(x_i \pm \delta x/2, y, t^n) \, \mathrm{d}y, \tag{16}$$

$$B_{y,i,j\pm1/2}^{n} \equiv \frac{1}{\delta x} \int_{x_i-\delta x/2}^{x_i+\delta x/2} B_y(x, y_i \pm \delta y/2, t^n) \, \mathrm{d}x \tag{17}$$

are averaged over the grid cell bounding faces and

$$\mathscr{E}_{z,i\pm1/2,j\pm1/2}^{n+1/2} \equiv \frac{1}{\delta t} \int_{t^n}^{t^{n+1}} \mathscr{E}_z(x_i \pm \delta x/2, y_i \pm \delta y/2, t) \, \mathrm{d}t \tag{18}$$

is averaged over the time interval δt. Note the fundamental representation of the magnetic field is an area-average at cell faces. Although CT-like difference formulae are possible based on volume averaged fields at cell centers [32], they preserve a discretization of the divergence on a different (larger) stencil than used to compute the fluxes.

Just as in finite volume methods, one typically approximates the electric field (flux) integral in Eq. (18) to some order of accuracy and applies Eqs. (14) and (15) to evolve the magnetic field components in time. Nevertheless, in a manner exactly analogous to the finite volume method, conservation of magnetic flux is strictly enforced, implying that the net magnetic charge interior to a grid cell vanishes at time t^{n+1} if it did so at time t^n. As such, the preservation of $\nabla \cdot \mathbf{B} = 0$ (in an integral sense) in the CT method is as fundamental as, e.g., the conservation of mass in a finite volume method. Moreover, in the CT approach, the magnetic field components are averaged over the smallest dimensional volume necessary so as to transform the differential equation into its integral form. In this way one maintains the maximal "point-wise" information possible, thereby minimizing the dissipation inherent in the averaging process.

2.3. Consistency of the CT and FV methods

To build a numerical scheme based on the CT method for the magnetic flux, and a FV method for the remaining conserved quantities, it is very important that the surface and volume averaged magnetic field components (and their fluxes) be coupled in a consistent manner. One common approach [3,11,28] (which we also follow) is to define the volume-averaged magnetic field components at cell centers as equal to the average of the area-averaged values at cell faces, i.e.

$$B_{x,i,j}^n = \frac{1}{2}\left(B_{x,i-1/2,j}^n + B_{x,i+1/2,j}^n\right), \tag{19}$$

$$B_{y,i,j}^n = \frac{1}{2}\left(B_{y,i,j-1/2}^n + B_{y,i,j+1/2}^n\right), \tag{20}$$

which is sufficient for second order accuracy. However, as shown below this choice implies a specific relationship between the numerical fluxes for the induction equation as integrated in the CT and FV formulations.

The expressions which describe the coupling of the fluxes in the CT and FV methods are a direct result of requiring that Eqs. (19) and (20) also hold at time t^{n+1}. Subtracting Eq. (19) from an equivalent expression at time t^{n+1}, and substituting Eqs. (9) and (14) for the time differences of the volume- and area-averaged magnetic field, respectively, we find

$$\hat{e}_{B_x} \cdot \left(F_{y,i,j-1/2}^{n+1/2} - F_{y,i,j+1/2}^{n+1/2}\right) = \frac{1}{2}\left(\mathscr{E}_{z,i-1/2,j-1/2}^{n+1/2} - \mathscr{E}_{z,i-1/2,j+1/2}^{n+1/2}\right) + \frac{1}{2}\left(\mathscr{E}_{z,i+1/2,j-1/2}^{n+1/2} - \mathscr{E}_{z,i+1/2,j+1/2}^{n+1/2}\right), \tag{21}$$

where $\hat{e}_{B_x}$ is a unit vector for the B_x component of the flux vector. It follows that

$$\hat{e}_{B_x} \cdot F_{y,i,j\pm1/2}^{n+1/2} = \frac{1}{2}\left(\mathscr{E}_{z,i-1/2,j\pm1/2}^{n+1/2} + \mathscr{E}_{z,i+1/2,j\pm1/2}^{n+1/2}\right), \tag{22}$$

which is consistent with the observation that the flux averages used in the finite volume method (Eq. (12)) are spatial averages of the electric fields used in the constrained transport method (Eq. (18)). Repeating this analysis for B_y we find

$$\hat{e}_{B_y} \cdot F_{x,i\pm1/2,j}^{n+1/2} = \frac{-1}{2}\left(\mathscr{E}_{z,i\pm1/2,j-1/2}^{n+1/2} + \mathscr{E}_{z,i\pm1/2,j+1/2}^{n+1/2}\right), \tag{23}$$

where $\hat{e}_{B_y}$ is a unit vector for the B_y component of the flux vector. Functionally, Eqs. (22) and (23) imply that one must replace the Godunov fluxes for the volume averaged x- and y-components of the magnetic field with the average of the corner centered $\mathscr{E}_z$, regardless of the details of the CT algorithm used to compute the latter. Thus, Eqs. (22) and (23) can be thought of as a corrector step that makes the predicted Godunov fluxes given by the Riemann solver consistent with the CT fluxes. Clearly, the CT algorithm used to compute the corner centered $\mathscr{E}_z$ will directly impact the accuracy and stability of the underlying Godunov scheme; in Section 3.2 we address the problem of constructing CT algorithms and the properties they should possess.

3. First order CT Godunov scheme

In this section we will construct and test a single step, two dimensional, first order integration algorithm based upon the PPM. The simplicity of this algorithm allows us to develop and test two of the most important elements of this paper: the calculation of the interface states in MHD and the systematic construction of CT algorithms. Moreover, the resulting algorithm (apart from the update step) is essentially the first half of the CTU + CT integration algorithm described in Section 4.

In Section 3.1 we describe the calculation of the interface states in the PPM algorithm for the system of ideal MHD. This interface state calculation involves a characteristic evolution of a dimensionally split system. In this step we will find the appearance of truly multidimensional terms in the induction equation which are proportional to $\partial B_x/\partial x$ and $\partial B_y/\partial y$. When these terms are included in the dimensionally split, linearized system of equations which are used to perform the characteristic evolution, they take the appearance of "source terms". We present two *gedanken* experiments which show that these multidimensional terms are essential to accurately predicting the time evolution in the interface states.

In Section 3.2 we address the question of the consistency of the CT algorithm with the underlying finite volume integration algorithm. Repeating the arguments which lead to Eqs. (22) and (23), we present an example of a CT algorithm which has insufficient dissipation and fails to reduce to the underlying integration algorithm for plane-parallel, grid-aligned flows. We proceed to describe a systematic approach to constructing a CT algorithm which can be applied with any approximate Riemann solver and reduces exactly to the underlying finite volume integration algorithm for plane-parallel, grid-aligned flows. In Section 3.3, we present a numerical study comparing three, surprisingly simple, CT algorithms each of which differs only in its dissipation for truly multidimensional problems.

3.1. Calculating the interface states

The algorithms presented in this paper are built upon the PPM. For a thorough discussion of PPM or its linear variant PLM and its implementation we refer the reader to the excellent descriptions in [8,24,29]. Roughly speaking the PPM algorithm can be broken down into three steps: spatial reconstruction, characteristic evolution, and flux evaluation. The purpose of these first two steps is to calculate a one-sided estimate of the time averaged state at the left- or right-hand sides of a particular grid cell interface. With these interface states in hand, the interface flux may be calculated via either an exact or approximate Riemann solver.

The calculation of the interface states in PPM is performed in primitive variables, and is a one-dimensional algorithm. However, in the two-dimensional (x,y) system of equations for ideal MHD there appear terms proportional to $\partial B_x/\partial x$ and $\partial B_y/\partial y$ which are not present in the truly one-dimensional system. In primitive variables, these terms only appear in the induction equation, which in component form is

$$\frac{\partial B_x}{\partial t} + \frac{\partial}{\partial y}\left(v_y B_x - B_y v_x\right) = 0, \tag{24}$$

$$\frac{\partial B_y}{\partial t} + \frac{\partial}{\partial x}\left(v_x B_y - B_x v_y\right) = 0, \tag{25}$$

$$\frac{\partial B_z}{\partial t} + \frac{\partial}{\partial x}\left(v_x B_z - B_x v_z\right) + \frac{\partial}{\partial y}\left(v_y B_z - B_y v_z\right) = 0. \tag{26}$$

Using the magnetic charge constraint ($\nabla \cdot \mathbf{B} = 0$) these terms can be eliminated from Eq. (26), giving

$$\frac{\partial B_z}{\partial t} + \frac{\partial}{\partial x}\left(v_x B_z\right) - B_x \frac{\partial v_z}{\partial x} + \frac{\partial}{\partial y}\left(v_y B_z\right) - B_y \frac{\partial v_z}{\partial y} = 0. \tag{27}$$

However, no such simplification can be made to Eqs. (24) and (25). It is natural to ask just how important these terms are and what role they play in the evolution of the magnetic field. A few *gedanken* experiments quickly show that they are absolutely essential, and at times are the dominant term in the equation.

Perhaps the most trivial example of a case in which these terms play an important role is for stationary solutions. As a concrete example, consider a circularly polarized Alfvén wave oriented at some oblique angle to the grid. One may always choose a reference frame in which the Alfvén wave is stationary. Because the wave is oriented oblique to the grid, $\partial B_x/\partial x$ and $\partial B_y/\partial y$ are non-zero throughout the domain (except at

extrema). In addition, for a standing Alfvén wave, the velocities are of the order of the Alfvén speed. In this case, the term $v_x(\partial B_y/\partial y)$ in Eq. (24) is not a small term and in fact, it must exactly balance the remaining term $\partial/\partial y(v_y B_x) - B_y(\partial v_x/\partial y)$ in order to hold the stationary solution. A similar situation also holds for Eq. (25).

As a second example, consider the simple advection of a magnetic field loop in the (x,y)-plane. Specifically, let $(\rho,P,\mathbf{v})$ = a constant with $\mathbf{v} = v_x\hat{\mathbf{i}}$, $B_z = 0$, and a circular magnetic field loop in the (x,y)-plane of sufficiently weak strength that $\beta = 2P/B^2 \gg 1$. This problem is equivalent to the advection of a passive scalar, the z-component of the magnetic vector potential. In this case Eqs. (24) and (25) are to a very good approximation given by

$$\frac{\partial B_x}{\partial t} - v_x\frac{\partial B_y}{\partial y} = 0, \tag{28}$$

$$\frac{\partial B_y}{\partial t} + v_x\frac{\partial B_y}{\partial x} = 0. \tag{29}$$

Hence it is clear that for this particular problem the term $v_x(\partial B_y/\partial y)$ is not only important, but completely controls the evolution of the x-component of the magnetic field.

We conclude that if the calculation of the interface states for multidimensional ideal MHD includes a characteristic evolution step, it is necessary to include the influence of the inherently multidimensional terms in the induction equation. Since PPM reconstruction includes a characteristic evolution step, we have found the following modifications necessary for multidimensional MHD.

We will restrict the description to a single spatial grid cell index i and consider the reconstruction process in the x-direction. We begin by calculating the primitive state vector, $V_i = \{\rho,v_x,v_y,v_z, B_x,B_y,B_z,P\}_i$ and $\tilde{V}_i$ such that $V_i = (\tilde{V}_i, B_{x,i})$, associated with q_i, the vector of the cell averaged conserved variables. Next, we apply the PPM algorithm to calculate the interface states of $\tilde{V}_i$ where the characteristic evolution step is calculated by solving

$$\frac{\partial \tilde{V}}{\partial t} + A\frac{\partial \tilde{V}}{\partial x} = \sigma, \tag{30}$$

where

$$\tilde{V} = \begin{pmatrix} \rho \\ v_x \\ v_y \\ v_z \\ B_y \\ B_z \\ P \end{pmatrix}, \quad \sigma = \begin{pmatrix} 0 \\ 0 \\ 0 \\ 0 \\ v_y(\partial B_x/\partial x) \\ 0 \\ 0 \end{pmatrix}, \tag{31}$$

$$A = \begin{pmatrix} v_x & \rho & 0 & 0 & 0 & 0 & 0 \\ 0 & v_x & 0 & 0 & B_y/\rho & B_z/\rho & 1/\rho \\ 0 & 0 & v_x & 0 & -B_x/\rho & 0 & 0 \\ 0 & 0 & 0 & v_x & 0 & -B_x/\rho & 0 \\ 0 & B_y & -B_x & 0 & v_x & 0 & 0 \\ 0 & B_z & 0 & -B_x & 0 & v_x & 0 \\ 0 & \gamma P & 0 & 0 & 0 & 0 & v_x \end{pmatrix}. \tag{32}$$

The matrix A is linearized about the state V_i and the source term σ is taken to be a constant with the only non-zero term evaluated as $v_{y,i}(B_{x,i+1/2} - B_{x,i-1/2})/\delta x$. Note that Eq. (30) includes all of the terms from Eq. (25). Denote the interface states calculated in this procedure as $\tilde{V}_{i+1/2}^{L}$ and $\tilde{V}_{i-1/2}^{R}$ where the superscripts (L,R) denote the left- or right-hand side of the interface to which they are adjacent. The final step is to define the primitive states $V_{i+1/2}^{L} = (\tilde{V}_{i+1/2}^{L}, B_{x,i+1/2})$ and $V_{i-1/2}^{R} = (\tilde{V}_{i-1/2}^{R}, B_{x,i-1/2})$. Note a further significant advantage of using face-centered (staggered) fields: the interface states of the longitudinal component of the magnetic field do not need to be reconstructed, and therefore will be continuous. Moreover, since monotonicity constraints associated with reconstruction are not applied, extrema in the longitudinal component of B at interfaces will be preserved.

The calculation of the y-interface states follows this same procedure, with the matrix A replaced by the equivalent one-dimensional wave matrix for the y-direction and the source term σ containing a non-zero entry for B_x equal to $v_x(\partial B_y/\partial y)$.

3.2. Constrained transport algorithms

In this section, we take up the problem of constructing CT algorithms. In order to identify the properties of a suitable CT algorithm, it is particularly interesting to consider the limiting case of plane-parallel, grid-aligned flows. In this limit $\partial B_x/\partial x = -\partial B_y/\partial y = 0$ so that there is no longer a difference between area and volume averaged magnetic fields. Moreover, if for example $\partial/\partial x = 0$ then the correct solution to the CT algorithm is readily obtained via symmetry, e.g. $\mathscr{E}_{z,i+1/2,j+1/2} = (\mathscr{E}_{z,i,j+1/2} + \mathscr{E}_{z,i+1,j+1/2})/2$. When a CT algorithm reduces to this, or an equivalent expression, for plane-parallel grid-aligned flows we describe it as being consistent with the underlying integration algorithm, since in this case it will give the identical solution as the underlying integration algorithm applied to the equivalent one-dimensional problem. Furthermore, we seek to construct CT algorithms which are compatible with any approximate Riemann solver, e.g. [5,10,14,20]. Hence, they should only depend upon the electric field in the flux vector, not on the structure of the waves which result from the solution of the Riemann problem.

3.2.1. Arithmetic averaging

Perhaps the simplest, and most often suggested, CT algorithm is based upon averaging the face centered electric fields obtained from the underlying integration algorithm, i.e. choose $\mathscr{E}_{z,i+1/2,j+1/2} = \bar{\mathscr{E}}_{z,i+1/2,j+1/2}$ where

$$\bar{\mathscr{E}}_{z,i+1/2,j+1/2} = \frac{1}{4}\left(\mathscr{E}_{z,i+1/2,j} + \mathscr{E}_{z,i+1/2,j+1} + \mathscr{E}_{z,i,j+1/2} + \mathscr{E}_{z,i+1,j+1/2}\right). \tag{33}$$

Unfortunately, this CT algorithm is not consistent with the underlying integration algorithm for plane-parallel, grid-aligned flows. This behavior is most easily understood when the underlying finite volume integration algorithm is unsplit.

Consider a plane-parallel, grid-aligned flow in which $\partial/\partial x = 0$. It follows that $\mathscr{E}_{z,i,j+1/2} = \mathscr{E}_{z,i+1,j+1/2}$ and $\mathscr{E}_{z,i+1/2,j} = \mathscr{E}_{z,i,j}$. Inserting these expressions into Eq. (33) we find

$$\bar{\mathscr{E}}_{z,i+1/2,j+1/2} = \frac{1}{4}\left(\mathscr{E}_{z,i,j} + \mathscr{E}_{z,i,j+1}\right) + \frac{1}{2}\mathscr{E}_{z,i,j+1/2}. \tag{34}$$

Contrast this with the correct solution, which by the assumption of planar symmetry is simply $\mathscr{E}_{z,i+1/2,j+1/2} = \mathscr{E}_{z,i,j+1/2}$. In order to assess the impact this CT algorithm has on the integration algorithm as a whole, let the FV numerical flux $F_{y,i,j+1/2}$ be written as

$$F_{y,i,j+1/2} = \frac{1}{2}\left(f_y(q_{i,j}) + f_y(q_{i,j+1}) + D_{i,j+1/2}(q_{i,j} - q_{i,j+1})\right), \tag{35}$$

where $D_{i,j+1/2}$ is the viscosity-matrix [18,14]. Contracting this expression with a unit vector $\hat{e}_{B_x}$ to extract the y-flux of B_x (remembering that $f_y(B_x) = \mathscr{E}_z$) we have the FV numerical electric field

$$\mathscr{E}_{z,i,j+1/2} = \frac{1}{2}(\mathscr{E}_{z,i,j} + \mathscr{E}_{z,i,j+1}) + \frac{1}{2}\hat{e}_{B_x}D_{i,j+1/2}(q_{i,j} - q_{i,j+1}). \tag{36}$$

Recall that, as discussed in Section 2.3, for FV + CT schemes this electric field is essentially a predictor value. To obtain the corrector value we begin by inserting the FV numerical electric field in Eq. (36) into the $\bar{\mathscr{E}}$ CT algorithm in Eq. (34) giving

$$\bar{\mathscr{E}}_{z,i+1/2,j+1/2} = \frac{1}{2}(\mathscr{E}_{z,i,j} + \mathscr{E}_{z,i,j+1}) + \frac{1}{4}\hat{e}_{B_x}D_{i,j+1/2}(q_{i,j} - q_{i,j+1}). \tag{37}$$

Note also that by symmetry we have $\bar{\mathscr{E}}_{z,i-1/2,j+1/2} = \bar{\mathscr{E}}_{z,i+1/2,j+1/2}$. Applying Eq. (22) we obtain the corrector value of the FV numerical electric field $\bar{\mathscr{E}}_{z,i,j+1/2} = \bar{\mathscr{E}}_{z,i+1/2,j+1/2}$ given by Eq. (37). Comparing Eq. (36) and (37) we find that the numerical viscosity is reduced by a factor of 2. Hence it is clear that with the arithmetic average CT algorithm $\bar{\mathscr{E}}$, the solution algorithm does not reduce to the underlying integration algorithm for plane-parallel, grid-aligned flows and the stability of this approach is questionable. The failure of this simple procedure to reduce to the underlying integration algorithm for plane-parallel, grid-aligned flows can be traced back to the lack of a directional bias in the averaging formula.

The arithmetic average CT algorithm formed the basis of an algorithm proposed by Balsara and Spicer [3]. The need for the CT algorithm to have a directional biasing was well understood by these authors. In their paper, they presented two switches which serve as local, multidimensional sensors for magnetosonic shocks. The authors then applied weighting coefficients which impart a directional bias to the CT algorithm.

However, the recognition that in Eq. (37) the viscous flux contribution to the corner value for $\mathscr{E}_z$ in the CT algorithm is simply too small by a factor of two, suggests that by doubling it we could recover the proper directional biasing. To that end we define

$$\hat{\mathscr{E}}_{z,i+1/2,j+1/2} \equiv 2\bar{\mathscr{E}}_{z,i+1/2,j+1/2} - \frac{1}{4}\left(\mathscr{E}_{z,i,j} + \mathscr{E}_{z,i,j+1} + \mathscr{E}_{z,i+1,j} + \mathscr{E}_{z,i+1,j+1}\right), \tag{38}$$

which can be written out explicitly as

$$\hat{\mathscr{E}}_{z,i+1/2,j+1/2} \equiv \frac{1}{2}\left(\mathscr{E}_{z,i+1/2,j} + \mathscr{E}_{z,i+1/2,j+1} + \mathscr{E}_{z,i,j+1/2} + \mathscr{E}_{z,i+1,j+1/2}\right)$$

$$- \frac{1}{4}\left(\mathscr{E}_{z,i,j} + \mathscr{E}_{z,i,j+1} + \mathscr{E}_{z,i+1,j} + \mathscr{E}_{z,i+1,j+1}\right). \tag{39}$$

Repeating the arguments leading to Eq. (34) using the CT algorithm defined by Eq. (39) one finds that the resulting scheme reduces to the underlying finite volume integration algorithm for plane-parallel, grid-aligned flows. It is not clear, however, from the ad-hoc construction described here how well such an algorithm will behave for truly multidimensional flows.

In the following section, we describe a systematic approach to constructing a CT algorithm which by design reverts to the underlying finite volume integration algorithm for plane-parallel, grid-aligned flows. Two entirely new CT algorithms will be constructed based upon different approximations. We will also find that the CT algorithm described by Eq. (39) can be understood as a limiting case of one of the CT algorithms constructed in the next section. Despite the simplicity of the CT algorithms constructed in the following section, we will see in Section 3.3 that they behave surprisingly well on multidimensional tests.

3.2.2. Systematic construction of CT algorithms

The approach described here is based upon the observation that a CT algorithm can be thought of as the inverse of the consistency relations given by Eqs. (22) and (23). In this sense, the CT algorithm can be thought of as a reconstruction, or integration procedure. Note that the interface fluxes which are calculated

as part of the base integration algorithm are midpoint values, centered spatially on the grid cell face, and averaged temporally over the time step. This suggests that we consider the CT algorithm, which calculates a time averaged value of $\mathscr{E}_z$ at the grid cell corner, to be a spatial integration procedure. For example, given a face centered value $\mathscr{E}_{z,i+1/2,j}$ we seek an estimate of $(\partial\mathscr{E}_z/\partial y)_{i+1/2,j+1/4}$ giving one value for

$$\mathscr{E}_{z,i+1/2,j+1/2} = \mathscr{E}_{z,i+1/2,j} + \frac{\delta y}{2}\left(\frac{\partial\mathscr{E}_z}{\partial y}\right)_{i+1/2,j+1/4}. \tag{40}$$

Clearly in two dimensions, one may integrate from any one of the four nearest face centers to the corner and generally the resulting values for $\mathscr{E}_{z,i+1/2,j+1/2}$ will differ. In the CT algorithms presented here, we will use the arithmetic average of these four values giving

$$\begin{aligned}
\mathscr{E}_{z,i+1/2,j+1/2} = &\frac{1}{4}\left(\mathscr{E}_{z,i+1/2,j} + \mathscr{E}_{z,i+1/2,j+1} + \mathscr{E}_{z,i,j+1/2} + \mathscr{E}_{z,i+1,j+1/2}\right) \\
&+ \frac{\delta y}{8}\left(\left(\frac{\partial\mathscr{E}_z}{\partial y}\right)_{i+1/2,j+1/4} - \left(\frac{\partial\mathscr{E}_z}{\partial y}\right)_{i+1/2,j+3/4}\right) \\
&+ \frac{\delta x}{8}\left(\left(\frac{\partial\mathscr{E}_z}{\partial x}\right)_{i+1/4,j+1/2} - \left(\frac{\partial\mathscr{E}_z}{\partial x}\right)_{i+3/4,j+1/2}\right). \tag{41}
\end{aligned}$$

The construction of this CT algorithm is completed by specifying a way to calculate the derivatives of $\mathscr{E}_z$ on the grid cell face.

To calculate $(\partial\mathscr{E}_z/\partial x)$ and $(\partial\mathscr{E}_z/\partial y)$ at grid cell faces, we propose to use an approximate solution for the evolution equations for $(\partial B_x/\partial x)$ and $(\partial B_y/\partial y)$. At a y-interface we differentiate the induction equation for B_x giving

$$\frac{\partial}{\partial t}\left(\frac{\partial B_x}{\partial x}\right) + \frac{\partial}{\partial y}\left(\frac{\partial\mathscr{E}_z}{\partial x}\right) = 0. \tag{42}$$

Similarly, at an x-interface we differentiate the induction equation for B_y giving

$$\frac{\partial}{\partial t}\left(\frac{\partial B_y}{\partial y}\right) - \frac{\partial}{\partial x}\left(\frac{\partial\mathscr{E}_z}{\partial y}\right) = 0. \tag{43}$$

Since these expression are still in conservation form it suggests that we may calculate an interface value for $(\partial\mathscr{E}_z/\partial x)$ at y-interfaces and $(\partial\mathscr{E}_z/\partial y)$ at x-interfaces using for example an HLL or Lax–Friedrichs flux. To evaluate these fluxes, we need estimates for the gradients of $(\partial\mathscr{E}_z/\partial x), (\partial\mathscr{E}_z/\partial y), (\partial B_x/\partial x)$ and $(\partial B_y/\partial y)$ on either side of the interface.

For the single step, CT Godunov algorithm which we are considering in this section, we calculate these derivatives as follows. For $(\partial B_x/\partial x)$ we difference the interface and cell center values giving

$$\left(\frac{\partial B_x}{\partial x}\right)_{i+1/4,j} = \frac{2}{\delta x}\left(B_{x,i+1/2,j} - B_{x,i,j}\right). \tag{44}$$

For $(\partial\mathscr{E}_z/\partial x)$ we difference the face centered $\mathscr{E}_{z,i+1/2,j}$ which comes directly from the Riemann solver and the cell center value $\mathscr{E}_{z,i,j}$ evaluated in the cell center state $q_{i,j}^n$ giving

$$\left(\frac{\partial\mathscr{E}_z}{\partial x}\right)_{i+1/4,j} = \frac{2}{\delta x}\left(\mathscr{E}_{z,i+1/2,j} - \mathscr{E}_{z,i,j}\right). \tag{45}$$

The values for $(\partial B_y/\partial y)$ and $(\partial\mathscr{E}_z/\partial y)$ are given by analogous expressions.

Pursuing the Lax–Friedrichs estimate with a maximum wave speed α we find

$$\left(\frac{\partial \mathscr{E}_z}{\partial x}\right)_{i+1/4,j+1/2} = \frac{1}{\delta x}\left(\mathscr{E}_{z,i+1/2,j} - \mathscr{E}_{z,i,j} + \mathscr{E}_{z,i+1/2,j+1} - \mathscr{E}_{z,i,j+1}\right)$$
$$+ \frac{\alpha}{\delta x}\left(B_{x,i+1/2,j} - B_{x,i,j} - B_{x,i+1/2,j+1} + B_{x,i,j+1}\right) \tag{46}$$

and

$$\left(\frac{\partial \mathscr{E}_z}{\partial y}\right)_{i+1/2,j+1/4} = \frac{1}{\delta y}\left(\mathscr{E}_{z,i,j+1/2} - \mathscr{E}_{z,i,j} + \mathscr{E}_{z,i+1,j+1/2} - \mathscr{E}_{z,i+1,j}\right)$$
$$+ \frac{\alpha}{\delta y}\left(B_{y,i+1,j+1/2} - B_{y,i+1,j} - B_{y,i,j+1/2} + B_{y,i,j}\right). \tag{47}$$

Repeating this procedure for the two remaining gradients and inserting the results into Eq. (41) we obtain

$$\mathscr{E}^\alpha_{z,i+1/2,j+1/2} = \frac{1}{2}\left(\mathscr{E}_{z,i,j+1/2} + \mathscr{E}_{z,i+1,j+1/2} + \mathscr{E}_{z,i+1/2,j} + \mathscr{E}_{z,i+1/2,j+1}\right)$$
$$- \frac{1}{4}\left(\mathscr{E}_{z,i,j} + \mathscr{E}_{z,i+1,j} + \mathscr{E}_{z,i,j+1} + \mathscr{E}_{z,i+1,j+1}\right)$$
$$+ \frac{\alpha}{8}\left(B_{x,i+1/2,j} - B_{x,i,j} - B_{x,i+1/2,j+1} + B_{x,i,j+1}\right)$$
$$+ \frac{\alpha}{8}\left(B_{x,i+1/2,j} - B_{x,i+1,j} - B_{x,i+1/2,j+1} + B_{x,i+1,j+1}\right)$$
$$+ \frac{\alpha}{8}\left(B_{y,i+1,j+1/2} - B_{y,i+1,j} - B_{y,i,j+1/2} + B_{y,i,j}\right)$$
$$+ \frac{\alpha}{8}\left(B_{y,i+1,j+1/2} - B_{y,i+1,j+1} - B_{y,i,j+1/2} + B_{y,i,j+1}\right). \tag{48}$$

One may readily show that for plane-parallel, grid-aligned flows, this CT algorithm will properly recover the associated one-dimensional solution for the underlying integration algorithm. Hereafter, we refer to Eq. (48) as the $\mathscr{E}^\alpha_z$ CT algorithm.

It is particularly interesting to note that the $\alpha = 0$ limit of Eq. (48) gives Eq. (39). Hence we may now understand Eq. (39) as being equivalent to the integration and averaging procedure described here with the approximation

$$\left(\frac{\partial \mathscr{E}_z}{\partial y}\right)_{i+1/2,j+1/4} = \frac{1}{2}\left(\frac{\partial \mathscr{E}_z}{\partial y}\right)_{i,j+1/4} + \frac{1}{2}\left(\frac{\partial \mathscr{E}_z}{\partial y}\right)_{i+1,j+1/4}. \tag{49}$$

Clearly this is not an upwinded approximation, suggesting that we should find some level of oscillations present in using this CT algorithm for multidimensional flows. However, since the dissipation arising from the terms proportional to α in the $\mathscr{E}^\alpha_z$ CT algorithm are only important for truly multidimensional flows, it is not clear if their neglect will have a substantive impact on the first order integration algorithm which we are considering here. For that reason, henceforth we will refer to the $\alpha = 0$ limit of the $\mathscr{E}^\alpha_z$ CT algorithm as $\mathscr{E}^\circ_z$, and include it in the tests in the following section.

We now have two CT algorithms: the $\mathscr{E}^\circ_z$ algorithm given by Eq. (39), and the $\mathscr{E}^\alpha_z$ algorithm given by Eq. (48). As our final CT algorithm, we note that for the special case of advection, $(\partial \mathscr{E}_z/\partial y)$ at an x-interface should be selected in an upwind fashion according to the contact mode. As such, we suggest that upwinding $(\partial \mathscr{E}_z/\partial y)$ at x-interfaces (and similarly $(\partial \mathscr{E}_z/\partial x)$ at y-interfaces) according to the contact mode may be sufficient to lead to a stable, non-oscillatory integration algorithm. Specifically, we choose

$$\left(\frac{\partial \mathscr{E}_z}{\partial y}\right)_{i+1/2,j+1/4} = \begin{cases} (\partial \mathscr{E}_z/\partial y)_{i,j+1/4} & \text{for } v_{x,i+1/2,j} > 0, \\ (\partial \mathscr{E}_z/\partial y)_{i+1,j+1/4} & \text{for } v_{x,i+1/2,j} < 0, \\ \frac{1}{2}\left((\partial \mathscr{E}_z/\partial y)_{i,j+1/4} + (\partial \mathscr{E}_z/\partial y)_{i+1,j+1/4}\right) & \text{otherwise.} \end{cases} \tag{50}$$

Note that this simply depends upon the sign of the mass flux, not the details of the solution of the Riemann problem at the interface and therefore can be applied with any approximate or exact Riemann solver. An analogous expression holds for the remaining three interface gradients of $\mathscr{E}_z$. We will refer to the CT algorithm which results from combining this approximation for the gradients of $\mathscr{E}_z$ with Eq. (41) as the $\mathscr{E}_z^c$ CT algorithm. By design this CT algorithm reduces to the underlying integration algorithm for plane-parallel grid-aligned flows and is properly upwinded in a multidimensional sense for the simple case of magnetic field advection.

In this section, we have presented a simple approach to constructing a CT algorithm which reduces exactly to the base integration algorithm for plane-parallel, grid-aligned flows. By design, the CT algorithms constructed here differ only in their numerical viscosity for multidimensional problems. It should be noted that the approach presented here can readily be incorporated into other numerical schemes, such as wave propagation algorithms [19]. The CT algorithms described here can also be applied to integration algorithms based upon spatial reconstruction to the grid cell corners as well [1]. While this might seem surprising following this presentation, note that the factors $(\delta x, \delta y)$ cancel in the $(\mathscr{E}_z^\alpha, \mathscr{E}_z^\circ, \mathscr{E}_z^c)$ CT algorithms. For such integration algorithms, the cell center value $\mathscr{E}_{z,i,j}$ should be replaced with the value of $\mathscr{E}_z$ calculated in the reconstructed fluid state at the grid cell corner, e.g. $q_{i+1/2,j+1/2}$. With this choice, the CT algorithms presented here will reduce to the base integration algorithms for plane-parallel, grid-aligned flows.

We note that another CT algorithm with the properties that it reduces to the base integration algorithm for plane-parallel, grid-aligned flows has recently been presented and tested elsewhere [23]. In particular, the authors of that paper present a general framework for combining CT and Godunov-type schemes and two specific implementations for their positive and central-type schemes. A direct comparison between their approach and ours is somewhat complex in the general case. In the specific case of a first order Godunov scheme, one can show (using Eqs. (41)–(47) in [23]) that their CT algorithm is identical to the $\mathscr{E}_z^\circ$ CT algorithm constructed here, although this is not immediately obvious from the description of their framework. For the more complex CT algorithms developed in our paper, it is likely that they too can be cast in the framework described by Londrillo and Del Zanna [23], although we have not attempted to do so.

3.3. First order CT Godunov tests

The integration algorithm utilized in this section is easily assembled from the elements described in the preceding sections. Starting at time t^n we calculate the x- and y-interface states as described in Section 3.1 using the PPM algorithm. Next, we use an approximate Riemann solver to calculate a flux at each grid cell interface. In the tests presented here we use a Roe linearization [5]. Finally, we apply one of the three $(\mathscr{E}_z^\alpha, \mathscr{E}_z^\circ, \mathscr{E}_z^c)$ CT algorithms. The resulting integration algorithm is first order accurate and subject to a restrictive CFL stability limit. In the tests presented in this section we use a time step

$$\delta t = 0.4 \min\left(\frac{\delta x}{|\lambda_x^{\max}|}, \frac{\delta y}{|\lambda_y^{\max}|}\right), \tag{51}$$

where $\lambda_{x,y}^{\max}$ indicates the fastest wave mode speed in the x- or y-direction.

3.3.1. Field loop advection

The first problem we consider is the advection of a weak magnetic field loop. The computational domain extends from $-1 \leqslant x \leqslant 1$, and $-0.5 \leqslant y \leqslant 0.5$, is resolved on a $2N \times N$ grid and has periodic boundary conditions on both x- and y-boundaries. For the tests presented in this section we take $N = 64$. The mass density $\rho = 1$ and the gas pressure $P = 1$. The velocity components $v_x = v_0 \cos(\theta)$, $v_y = v_0 \sin(\theta)$, $v_z = 0$ where $\cos(\theta) = 2/\sqrt{5}$ and $\sin(\theta) = 1/\sqrt{5}$. In the diffusion tests we set $v_0 = 0$ while in the advection tests we set $v_0 = \sqrt{5}$ so that by $t = 1$ the field loop will have been advected around the grid one complete orbit along

the grid diagonal. The z-component of the magnetic field $B_z = 0$ while the in plane components B_x and B_y are initialized from the z-component of the magnetic vector potential where

$$A_z \equiv \begin{cases} A_0(R-r) & \text{for } r \leqslant R, \\ 0 & \text{for } r > R, \end{cases} \tag{52}$$

where $A_0 = 10^{-3}$, $R = 0.3$ and $r = \sqrt{x^2 + y^2}$. Thus for $r \leqslant R$, $\beta = 2P/B^2 = 2 \times 10^6$ and the magnetic field is essentially a passive scalar.

In the first test we consider the diffusion of the field loop. In Fig. 1, we compare gray-scale images of the magnetic pressure $(B_x^2 + B_y^2)$ at $t = 0$ to the evolved results at $t = 2$ using the three $(\mathscr{E}_z^\alpha, \mathscr{E}_z^\circ, \mathscr{E}_z^c)$ CT algorithms. Clearly, the $\mathscr{E}_z^\circ$ CT algorithm leads to an unacceptable amount of diffusion compared to the other two, as evidenced by the emergence of a hole at the center caused by reconnection. The $(\mathscr{E}_z^\circ, \mathscr{E}_z^c)$ CT algorithms lead to essentially identical results and a very small amount of diffusion. Apparently the additional dissipation included in the $\mathscr{E}_z^\alpha$ CT algorithm is not necessary for stability in this test.

Next, we consider the advection of the magnetic field loop. Unlike in the stationary field loop test, here the evolved results appear quite similar for the $\mathscr{E}_z^\alpha$ and $\mathscr{E}_z^c$ CT algorithms. In Fig. 2, we present gray-scale images of the magnetic pressure at $t = 0.19$ for the three $(\mathscr{E}_z^\alpha, \mathscr{E}_z^\circ, \mathscr{E}_z^c)$ CT algorithms. At this time, the $\mathscr{E}_z^\alpha$ and $\mathscr{E}_z^c$ CT algorithms give quite similar results. In contrast, the $\mathscr{E}_z^\circ$ CT algorithm appears to have insufficient dissipation leading to an oscillatory solution. These observations are consistent with the comments in Section 3.2.2 regarding the upwinding of the gradients of $\mathscr{E}_z$ at the interfaces. In Fig. 3, we present gray-scale images of the magnetic pressure at $t = 2$ for the three $(\mathscr{E}_z^\alpha, \mathscr{E}_z^\circ, \mathscr{E}_z^c)$ CT algorithms. By this time the oscillations present using the $\mathscr{E}_z^\circ$ CT algorithm have come to dominate the solution. The results from the $\mathscr{E}_z^\alpha$ and $\mathscr{E}_z^c$ CT algorithms continue to remain quite similar, implying that the dissipation of the first order scheme is comparable to the dissipation in the $\mathscr{E}_z^\alpha$ CT algorithm. Note also the similarity to the magnetic pressure image in Fig. 1 for the $\mathscr{E}_z^\alpha$ CT algorithm.

From the results of these tests we are led to conclude that of the three algorithms, the $\mathscr{E}_z^c$ CT algorithm is preferable. The $\mathscr{E}_z^\alpha$ CT algorithm leads to stable, yet diffusive results for stationary problems. The $\mathscr{E}_z^\circ$ CT algorithm appears to have insufficient dissipation for advection problems leading to oscillatory results. One might naturally wonder, however, if these results are biased to favor the $\mathscr{E}_z^c$ CT algorithm by design.
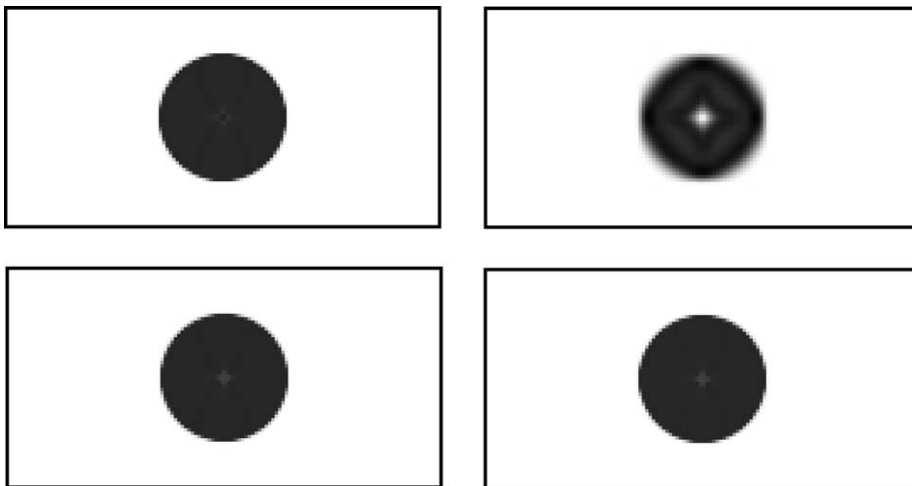

Fig. 1. Gray-scale images of the magnetic pressure $(B_x^2 + B_y^2)$ at $t = 0$ (top left) and at $t = 2$ for a stationary medium ($v_0 = 0$) using the $\mathscr{E}_z^\alpha$ (top right), the $\mathscr{E}_z^\circ$ (bottom left) and the $\mathscr{E}_z^c$ (bottom right) CT algorithm.
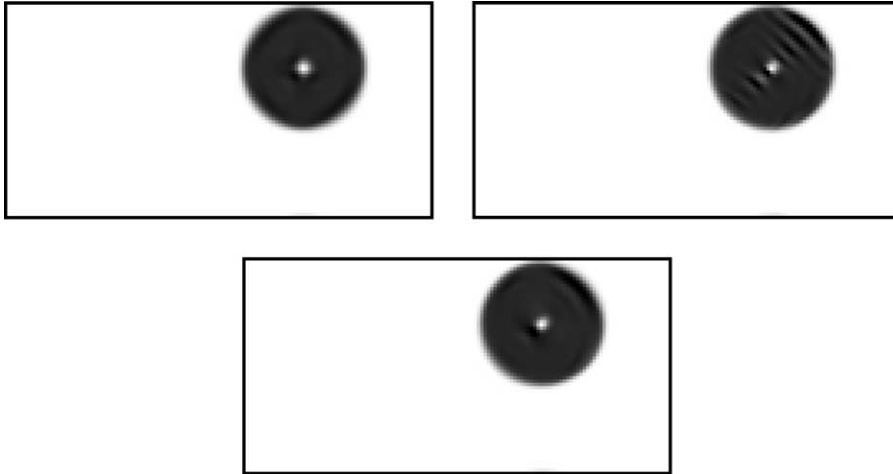
Fig. 2. Gray-scale images of the magnetic pressure $(B_x^2 + B_y^2)$ at $t = 0.19$ for an advected field loop $(v_0 = \sqrt{5})$ using the $\mathscr{E}_z^\alpha$ (top left), $\mathscr{E}_z^\circ$ (top right) and $\mathscr{E}_z^c$ (bottom) CT algorithm.

In the following section, we present additional tests of these CT algorithms where wave modes other than the contact mode play an important role in the solution. We note in passing that the source terms described in Section 3.1 are absolutely essential to obtain the results presented here. If they had been omitted, the field loop disintegrates in oscillations before completing a fraction of an orbital period.

3.3.2. Circularly polarized Alfvén wave

In a recent paper Tóth [32] described a test problem involving the evolution of traveling and standing circularly polarized Alfvén waves in a periodic domain. This test problem is interesting from the point of view that the initial conditions are nonlinear solutions to the equations of ideal MHD. Unfortunately,
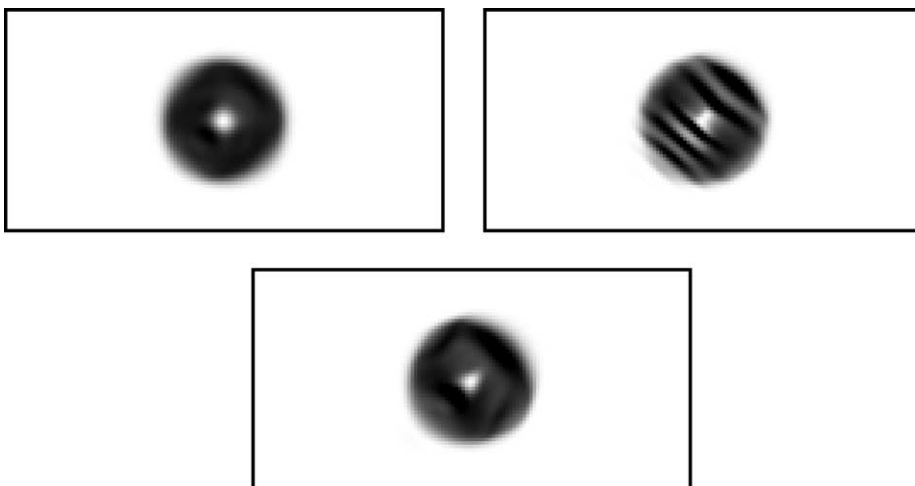

Fig. 3. Gray-scale images of the magnetic pressure $(B_x^2 + B_y^2)$ at $t = 2$ for an advected field loop $(v_0 = \sqrt{5})$ using the $\mathscr{E}_z^\alpha$ (top left), $\mathscr{E}_z^\circ$ (top right) and $\mathscr{E}_z^c$ (bottom) CT algorithm.

their efficacy as a discriminating test for multidimensional MHD codes has been hindered slightly [23,25] by the fact that they are susceptible to a parametric instability [17,13]. Nevertheless, we have found this to be a useful test and find no indication of instability for the parameters adopted here.

The initial conditions we utilize here are slightly different than in the original description [32]. The computational domain extends from $0 \leqslant x \leqslant \sqrt{5}$, and $0 \leqslant y \leqslant \sqrt{5}/2$ is resolved on a $2N \times N$ grid and has periodic boundary conditions on both x- and y-boundaries. For the tests presented in this section we take $N = 8$. The Alfvén wave propagates at an angle $\theta = \tan^{-1}(2) \approx 63.4°$ with respect to the x-axis and has a wavelength $\lambda = 1$. The mass density $\rho = 1$ and the gas pressure $P = 0.1$. The velocity and magnetic field components are most easily described in a rotated coordinate system

$$x_1 = x \cos \theta + y \sin \theta, \tag{53}$$

$$x_2 = -x \sin \theta + y \cos \theta, \tag{54}$$

$$x_3 = z \tag{55}$$

such that the Alfvén wave propagates along the x_1 axis. The magnetic field components $B_1 = 1$, $B_2 = 0.1$ $\sin(2\pi x_1)$, and $B_3 = 0.1 \cos(2\pi x_1)$. The velocity components $v_1 = (0,1)$ for traveling or standing Alfvén waves, respectively, $v_2 = 0.1 \sin(2\pi x_1)$, and $v_3 = 0.1 \cos(2\pi x_1)$. With this set of initial conditions and $v_1 = 0$ the Alfvén wave will travel a distance of one wavelength λ in a time $t = 1$.

To better illustrate the geometry of this problem, a high resolution image of the out of plane component of the magnetic field, B_z is presented in Fig. 4. Also included in this figure is an image of B_z for the resolution tested ($N = 8$) in order to emphasize that the coarsest resolution for this wave is in the y-direction (with only eight grid points per wavelength), and that there are essentially two complete wavelengths across the grid diagonal. We have found that low resolution tests such as presented below are much more informative, since differences between algorithms are generally largest in this case. Note that, just as in the field loop problem, the in-plane components of the magnetic field (B_x,B_y) are initialized via the z-component of the appropriate magnetic vector potential.

In Tóth's analysis [32] he found that the errors in the solution were dominated by errors in the transverse magnetic field B_2 and velocity v_2 in our notation. He presented line plots of B_2 versus x as a function of resolution and numerical scheme. In Fig. 5, we present analogous line plots of B_2 versus x_1 for the case of a standing and traveling waves including the initial conditions at $t = 0$ and the solutions at $t = 5$ for the three CT algorithms under study. It is worth noting that in these plots we have calculated B_2 using the cell center magnetic fields and have included the data for every grid cell in the calculation. Owing to the angle of the wave with respect to the grid, there are many data points which fall on a single x_1 position. The lack of scatter in the data shows that the Alfvén wave retains its planar structure extremely well for the duration of the calculation.
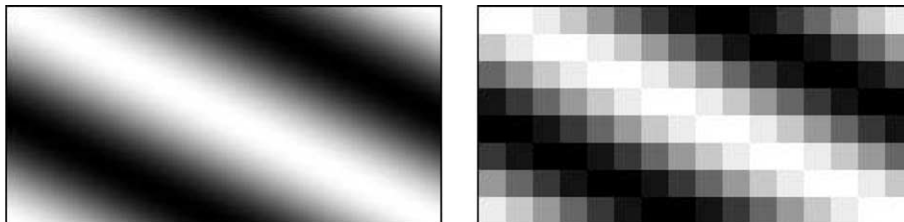

Fig. 4. Plot of B_z at the initial time for the circularly polarized Alfvén wave problem at high resolution, $N = 128$, (left) and at the resolution plotted in Fig. 5 (right).
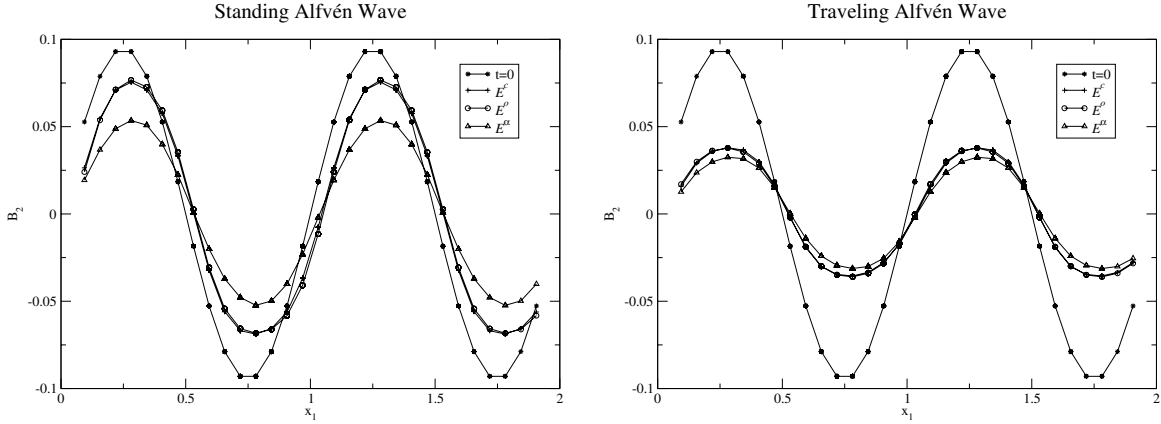
Standing Alfvén Wave   Traveling Alfvén Wave

Fig. 5. Plot of B_2 versus x_1 for the standing (left) and traveling (right) circularly polarized Alfvén wave problem at $t = 0$ and $t = 5$ for the three ($\mathscr{E}_z^\alpha, \mathscr{E}_z^\circ, \mathscr{E}_z^c$) CT algorithms.

Comparing the plots of B_2 versus x_1 for the three CT algorithms, we generally find that the $\mathscr{E}_z^\circ$ or $\mathscr{E}_z^c$ CT algorithm give nearly identical results, while the $\mathscr{E}_z^\alpha$ CT algorithm is more dissipative. In the case of the standing wave solution, the dissipation rate in the $\mathscr{E}_z^\alpha$ CT algorithm is approximately twice that of the other two. In the traveling wave case, the difference in the dissipation rate is much less indicating that the dissipation in the first order integration algorithm is comparable.

From these tests, and many additional tests not included here, we conclude that the $\mathscr{E}_z^c$ CT algorithm has the best dissipation properties. The $\mathscr{E}_z^\alpha$ CT algorithm gives stable, yet diffusive results while the $\mathscr{E}_z^\circ$ CT algorithm appears to have insufficient dissipation, leading to oscillatory results for advection problems. These observations suggest that the $\mathscr{E}_z^\alpha$ CT algorithm with α set equal to some estimate of the magnitude of the local gas velocity could also lead to a non-oscillatory CT algorithm. This idea is however untested, nor is it clear that it would result in an algorithm which is superior to the $\mathscr{E}_z^c$ CT algorithm. For the remainder of this paper we will use the $\mathscr{E}_z^c$ CT algorithm in test problems.

4. Second order CTU + CT Godunov scheme

The CTU method was developed by Colella as an unsplit, two-dimensional sequel to the PPM of Colella and Woodward for Euler's equations. The algorithm is second order accurate and degenerates to the base PPM algorithm for plane-parallel, grid-aligned flows. Formally, the algorithm can be described in just a few steps.

First, one calculates left and right interface states at each grid cell face using the one-dimensional algorithm from the base PPM scheme. Using the notation adopted in Section 3.1, let these be denoted by $(q_{i+1/2,j}^{L*}, q_{i+1/2,j}^{R*}, q_{i,j+1/2}^{L*}, q_{i,j+1/2}^{R*})$. For MHD, the PPM interpolation used to construct these states must include all the multidimensional terms identified in Section 3.1. At each interface one solves the Riemann problem associated with these interface states and computes the fluxes $(F_{x,i+1/2,j}^*, F_{y,i,j+1/2}^*)$. Next, one updates the interface states to the 1/2 time step

$$q_{i+1/2,j}^L = q_{i+1/2,j}^{L*} - \frac{1}{2}\frac{\delta t}{\delta y}\left(F_{y,i,j+1/2}^* - F_{y,i,j-1/2}^*\right), \tag{56}$$

$$q_{i+1/2,j}^R = q_{i+1/2,j}^{R*} - \frac{1}{2}\frac{\delta t}{\delta y}\left(F_{y,i+1,j+1/2}^* - F_{y,i+1,j-1/2}^*\right), \tag{57}$$

$$q_{i,j+1/2}^{\mathrm{L}} = q_{i,j+1/2}^{\mathrm{L}*} - \frac{1}{2} \frac{\delta t}{\delta x} \left(F_{x,i+1/2,j}^{*} - F_{x,i-1/2,j}^{*} \right), \tag{58}$$

$$q_{i,j+1/2}^{\mathrm{R}} = q_{i,j+1/2}^{\mathrm{R}*} - \frac{1}{2} \frac{\delta t}{\delta x} \left(F_{x,i+1/2,j+1}^{*} - F_{x,i-1/2,j+1}^{*} \right). \tag{59}$$

Solving the Riemann problem associated with the four updated interface states $(q_{i+1/2,j}^{\mathrm{L,R}}, q_{i,j+1/2}^{\mathrm{L,R}})$ one obtains second order accurate fluxes which can be used to update $q_{i,j}$ via the standard finite volume integration relation, Eq. (9).

Unfortunately, the CTU method as just described is incomplete for MHD when using constrained transport. One reason is that Eqs. (56)–(59) fail to preserve the $\nabla \cdot \mathbf{B} = 0$ condition. The marriage of CTU with CT for MHD requires a modification of Eqs. (56)–(59) for updating the interface states, and an additional CT integration step for updating $q_{i,j}^{n}$ from time t^{n} to t^{n+1}.

4.1. Updating the interface states

There are two modifications to the CTU method required for MHD using CT. The first modification, required by constrained transport, is that the fluxes $(F_{x,i+1/2,j}^{*}, F_{y,i,j+1/2}^{*})$ must be integrated from face center, to the grid cell corner. Hence from the interface centered flux $F_{x,i+1/2,j}^{*}$ we obtain two corner centered fluxes $(F_{x,i+1/2,j+1/2}^{\mathrm{L}*}, F_{x,i+1/2,j-1/2}^{\mathrm{R}*})$ where the superscript L,R indicates that the fluxes have been integrated from face center to the grid cell corner from either the left $(-y)$ or right $(+y)$ side of the grid cell corner. The labeling of the y-fluxes $(F_{y,i+1/2,j+1/2}^{\mathrm{L}*}, F_{y,i-1/2,j+1/2}^{\mathrm{R}*})$ obtained from $F_{y,i,j+1/2}^{*}$ follows an analogous convention. The second modification, originating from differences in the form of the equations of ideal MHD when written in primitive, or conservative variables, is the addition of source terms. The modified form of the update relations in Eqs. (56)–(59) for advancing the interface states to the 1/2 time step can be formally written as

$$q_{i+1/2,j}^{\mathrm{L}} = q_{i+1/2,j}^{\mathrm{L}*} - \frac{1}{2} \frac{\delta t}{\delta y} \left(F_{y,i+1/2,j+1/2}^{\mathrm{L}*} - F_{y,i+1/2,j-1/2}^{\mathrm{L}*} \right) + \frac{\delta t}{2} S_{x,i,j}, \tag{60}$$

$$q_{i+1/2,j}^{\mathrm{R}} = q_{i+1/2,j}^{\mathrm{R}*} - \frac{1}{2} \frac{\delta t}{\delta y} \left(F_{y,i+1/2,j+1/2}^{\mathrm{R}*} - F_{y,i+1/2,j-1/2}^{\mathrm{R}*} \right) + \frac{\delta t}{2} S_{x,i+1,j}, \tag{61}$$

$$q_{i,j+1/2}^{\mathrm{L}} = q_{i,j+1/2}^{\mathrm{L}*} - \frac{1}{2} \frac{\delta t}{\delta x} \left(F_{x,i+1/2,j+1/2}^{\mathrm{L}*} - F_{x,i-1/2,j+1/2}^{\mathrm{L}*} \right) + \frac{\delta t}{2} S_{y,i,j}, \tag{62}$$

$$q_{i,j+1/2}^{\mathrm{R}} = q_{i,j+1/2}^{\mathrm{R}*} - \frac{1}{2} \frac{\delta t}{\delta x} \left(F_{x,i+1/2,j+1/2}^{\mathrm{R}*} - F_{x,i-1/2,j+1/2}^{\mathrm{R}*} \right) + \frac{\delta t}{2} S_{y,i,j+1}. \tag{63}$$

The procedure for integrating the fluxes from face center to grid cell corner, and the need for the source terms will now be described in turn.

4.1.1. Integrating the fluxes to the grid cell corner

Recall that $f_x(B_y) = -\mathscr{E}_z$ and $f_y(B_x) = \mathscr{E}_z$ and let $\hat{e}_{B_x}$ and $\hat{e}_{B_y}$ denote the unit vectors for the B_x and B_y components of the flux vector. Furthermore, let $\mathscr{E}_{z,i,j+1/2}^{*} = \hat{e}_{B_x} \cdot F_{y,i,j+1/2}^{*}$ and $\mathscr{E}_{z,i+1/2,j}^{*} = -\hat{e}_{B_y} \cdot F_{x,i+1/2,j}^{*}$. This allows us to define

$$F_{y,i+1/2,j+1/2}^{\mathrm{L}*} = F_{y,i,j+1/2}^{*} + (\mathscr{E}_{z,i+1/2,j+1/2}^{*} - \mathscr{E}_{z,i,j+1/2}^{*}) \hat{e}_{B_x}, \tag{64}$$

$$F_{y,i+1/2,j+1/2}^{\mathrm{R}*} = F_{y,i+1,j+1/2}^{*} + (\mathscr{E}_{z,i+1/2,j+1/2}^{*} - \mathscr{E}_{z,i+1,j+1/2}^{*}) \hat{e}_{B_x}, \tag{65}$$

$$F_{x,i+1/2,j+1/2}^{\mathrm{L}*} = F_{x,i+1/2,j}^{*} - (\mathscr{E}_{z,i+1/2,j+1/2}^{*} - \mathscr{E}_{z,i+1/2,j}^{*}) \hat{e}_{B_y}, \tag{66}$$

$$F_{x,i+1/2,j+1/2}^{R*} = F_{x,i+1/2,j+1}^{*} - (\mathscr{E}_{z,i+1/2,j+1/2}^{*} - \mathscr{E}_{z,i+1/2,j+1}^{*})\hat{e}_{B_y}. \tag{67}$$

From a practical point of view, integrating the fluxes from face center to grid cell corner in this fashion can be thought of as simply stating that the normal components of the magnetic field at grid cell interfaces is advanced to time $t^{n+1/2}$ via a CT integral. Namely,

$$B_{x,i\pm1/2,j}^{n+1/2} = B_{x,i\pm1/2,j}^{n} + \frac{1}{2}\frac{\delta t}{\delta y}\left(\mathscr{E}_{z,i\pm1/2,j-1/2}^{*} - \mathscr{E}_{z,i\pm1/2,j+1/2}^{*}\right). \tag{68}$$

$$B_{y,i,j\pm1/2}^{n+1/2} = B_{y,i,j\pm1/2}^{n} - \frac{1}{2}\frac{\delta t}{\delta x}\left(\mathscr{E}_{z,i-1/2,j\pm1/2}^{*} - \mathscr{E}_{z,i+1/2,j\pm1/2}^{*}\right). \tag{69}$$

The last part of this integration procedure which requires description is the CT algorithm used to calculate the corner centered emf $\mathscr{E}_{z,i+1/2,j+1/2}^{*}$. To accomplish this, note that the fluxes $(F_{x,i+1/2,j}^{*}, F_{y,i,j+1/2}^{*})$ are equivalent to the fluxes used in the single step integration algorithm tested in Section 3.3. As such, the calculation of the corner centered emf $\mathscr{E}_{z,i+1/2,j+1/2}^{*}$ may be accomplished with any of the $(\mathscr{E}_z^{\alpha}, \mathscr{E}_z^{\circ}, \mathscr{E}_z^{c})$ CT algorithms described in Section 3.2. For the tests problems presented in the following sections we will use the $\mathscr{E}_z^{c}$ CT algorithm. We note that following this procedure, the magnetic fields satisfy the $\nabla \cdot \mathbf{B} = 0$ condition at time $t^{n+1/2}$.

4.1.2. Interface state MHD source terms

The source terms present in Eqs. (60)–(63) follow from the recognition that if they are set to zero, the updated interface states are not formally advanced by $\delta t/2$ for MHD. The basic reason for this discrepancy lies in the fact that the interface states as described in Section 3.1 (and typically implemented in PPM) are calculated in primitive variables. As a result,

$$q_{i+1/2,j}^{L*} \neq q(x_i + \delta x/2, y_j) - \frac{\delta t}{2}\frac{\partial f_x}{\partial x} \tag{70}$$

and similarly for the other interface states. To correct this situation, we define

$$S_{x,i,j} \equiv \begin{pmatrix} 0 \\ B_{x,i,j}^{n} \\ B_{y,i,j}^{n} \\ B_{z,i,j}^{n} \\ 0 \\ 0 \\ v_{z,i,j}^{n} \\ B_{z,i,j}^{n} v_{z,i,j}^{n} \end{pmatrix} \left(\frac{B_{x,i+1/2,j}^{n} - B_{x,i-1/2,j}^{n}}{\delta x}\right) \tag{71}$$

and

$$S_{y,i,j} \equiv \begin{pmatrix} 0 \\ B_{x,i,j}^{n} \\ B_{y,i,j}^{n} \\ B_{z,i,j}^{n} \\ 0 \\ 0 \\ v_{z,i,j}^{n} \\ B_{z,i,j}^{n} v_{z,i,j}^{n} \end{pmatrix} \left(\frac{B_{y,i,j+1/2}^{n} - B_{y,i,j-1/2}^{n}}{\delta y}\right). \tag{72}$$

With this choice, the interface states as updated by Eqs. (60)–(63) include all of the necessary terms so as to be advanced to time $t^{n+1/2}$.

Note that the choice to include the term $v_z(\partial B_x/\partial x)$ for B_z (and the associated energy source term) at the x-interfaces in this step, rather than including it when calculating the interface states as described in Section 3.1 has a very important consequence; it prevents an erroneous field growth of B_z in certain circumstances. To elucidate this situation, consider a magnetic field loop in the (x,y)-plane advected with a uniform $\mathbf{v} = v_z\hat{\mathbf{k}}$ and set $B_z = 0$ initially. With the exception of extrema, $\partial B_x/\partial x$ and $\partial B_y/\partial y$ are non-zero throughout the field loop. However, since v_z is uniform the magnetic field B_z should remain equal to zero. If the term $v_z\partial B_x/\partial x$ is included when calculating the x-interface states in Section 3.1 they would contain a non-zero B_z. Owing to the coherent structure of the in-plane field loop, the the values of B_z in the interface states will also have a coherent structure. Upon updating the interface states with the transverse flux gradients, the growth of B_z is diminished, however it is not canceled identically. The net result is an unphysical growth of a coherent B_z which eventually influences the in-plane dynamics. The choice of source terms described in Section 3.1 and this section maintains B_z to the level of roundoff error with an incoherent structure. Hence, the algorithm presented here accurately captures the balance of the terms proportional to $\partial B_x/\partial x$ and $\partial B_y/\partial y$, as described in Section 3.1, in both the predictor and corrector steps for calculating the interface state values of B_z.

4.2. The constrained transport update algorithm

After having updated the interface states to time $t^{n+1/2}$ via Eqs. (60)–(63), the interface flux calculation is repeated giving rise to the second order accurate fluxes $(F_{x,i+1/2,j}^{n+1/2}, F_{y,i,j+1/2}^{n+1/2})$. In the CTU algorithm, this set of fluxes is used to evolve $q_{i,j}^n$ to time t^{n+1}. However, in order to evolve the magnetic fields via constrained transport, we must extend the CT algorithms described in Section 3.2. Requiring that the algorithm reduce to the base integration algorithm for plane-parallel, grid-aligned flows we find that we simply need to advance the electric field gradient calculation to the half time step, i.e. Eq. (45) is replaced with

$$\left(\frac{\partial \mathscr{E}_z}{\partial x}\right)_{i+1/4,j}^{n+1/2} = \frac{2}{\delta x}\left(\mathscr{E}_{z,i+1/2,j}^{n+1/2} - \mathscr{E}_{z,i,j}^{n+1/2}\right). \tag{73}$$

The electric field $\mathscr{E}_{z,i,j}^{n+1/2}$ is the cell center value advanced by $\delta t/2$, that is

$$\mathscr{E}_{z,i,j}^{n+1/2} = v_{y,i,j}^{n+1/2} B_{x,i,j}^{n+1/2} - v_{x,i,j}^{n+1/2} B_{y,i,j}^{n+1/2}, \tag{74}$$

where to be consistent with the integration scheme, the cell center magnetic fields are given by

$$B_{x,i,j}^{n+1/2} = \frac{1}{2}\left(B_{x,i-1/2,j}^{n+1/2} + B_{x,i+1/2,j}^{n+1/2}\right), \tag{75}$$

$$B_{y,i,j}^{n+1/2} = \frac{1}{2}\left(B_{y,i,j-1/2}^{n+1/2} + B_{y,i,j+1/2}^{n+1/2}\right), \tag{76}$$

where the field components on the right-hand side of these equations are equal to the normal components of the magnetic field in the interface states $(q_{i\pm1/2,j}^{L,R}, q_{i,j\pm1/2}^{L,R})$. The density, x- and y-momenta needed to compute the velocity components in Eq. (74) are advanced by $\delta t/2$ using

$$q_{i,j}^{n+1/2} = q_{i,j}^n + \frac{1}{2}\frac{\delta t}{\delta x}\left(F_{x,i-1/2,j}^* - F_{x,i+1/2,j}^*\right) + \frac{1}{2}\frac{\delta t}{\delta y}\left(F_{y,i,j-1/2}^* - F_{y,i,j+1/2}^*\right), \tag{77}$$

where the fluxes are those calculated in the first step of the CTU algorithm.

4.3. Summary

The following steps summarize the CTU + CT algorithm for MHD:

(1) Calculate the x- and y-interface states $(q^{L*}_{i+1/2,j}, q^{R*}_{i+1/2,j}, q^{L*}_{i,j+1/2}, q^{R*}_{i,j+1/2})$ using the PPM algorithm, and the multidimensional source terms as described by Eqs. (30)–(32) in Section 3.1.
(2) Calculate the x- and y-interface fluxes $(F^*_{x,i+1/2,j}, F^*_{y,i,j+1/2})$ associated with the interface states $(q^{L*,R*}_{i+1/2,j}, q^{L*,R*}_{i,j+1/2})$ via a Riemann solver.
(3) Using the $\mathscr{E}^c_z$ CT algorithm described in Eqs. (41) and (50) integrate the face centered fluxes to the grid cell corner as described in Section 4.1.1.
(4) Compute the the four updated interface states $(q^{L,R}_{i+1/2,j}, q^{L,R}_{i,j+1/2})$ via Eqs. (60)–(63) with the source terms detailed in Section 4.1.2.
(5) Compute the x- and y-interface fluxes $(F^{n+1/2}_{x,i+1/2,j}, F^{n+1/2}_{y,i,j+1/2})$ associated with the interface states $(q^{L,R}_{i+1/2,j}, q^{L,R}_{i,j+1/2})$ via a Riemann solver.
(6) Compute the grid cell corner centered electric field $\mathscr{E}^{n+1/2}_{z,i+1/2,j+1/2}$ using the $\mathscr{E}^c_z$ CT algorithm described in Eqs. (41) and (50) advanced to time $t^{n+1/2}$ as described in Section 4.2.
(7) Advance the surface averaged normal components of the magnetic field from time t^n to t^{n+1} using Eqs. (14) and (15).
(8) Advance the remaining volume averaged conserved quantities from time t^n to t^{n+1} using Eq. (9).

This completes the description of the algorithm. It is second order accurate, unsplit, and preserves the $\nabla \cdot \mathbf{B} = 0$ constraint throughout the time step. In the following section we apply this CTU + CT scheme to a variety of test problems.

5. Tests

In this section, we present results obtained with the CTU + CT integration algorithm just described. Throughout these tests we use the $\mathscr{E}^c_z$ CT algorithm.

5.1. Field loop advection

The advection of a magnetic field loop discussed in Section 3.3.1 was instructive for assessing the dissipation in the different CT algorithms. In this subsection, we present the results obtained for this problem with the second-order CTU + CT algorithm. The grid resolution and initial conditions are equivalent to those used in Section 3.3.1.

In Fig. 6, we present gray-scale images of B^2 at times $t = 0$ and $t = 2$. Comparing these figures we find that the majority of the field dissipation has occurred at the center and boundaries of the field loop, where
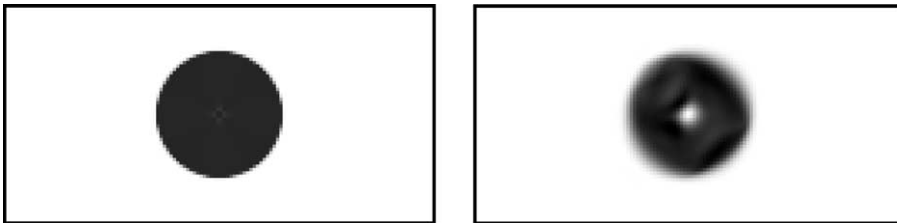

Fig. 6. Gray-scale images of the magnetic pressure $(B^2_x + B^2_y)$ at $t = 0$ (left) and $t = 2$ (right) using the CTU + CT integration algorithm.

the current density is initially singular. A more quantitative measure of the magnetic field dissipation rate is given by the time evolution of the volume average of B^2 as shown in Fig. 7. We find that the measured values (denoted by symbols) is well described by a power law (solid line) of the form $B^2 = A(1 - (t/\tau)^\alpha)$ with $A = 3.463 \times 10^{-8}$, $\tau = 10.614 \times 10^3$ and $\alpha = 0.2914$.

Another important indicator of the properties of the integration algorithm is the geometry of the magnetic field lines. Note that since the CT method evolves the interface magnetic flux (preserving $\nabla \cdot \mathbf{B} = 0$) one may readily integrate to find the z-component of the magnetic vector potential. The magnetic field lines presented in Fig. 8 are obtained by contouring A_z. The same values of A_z are used for the contours in both the $t = 0$ and the $t = 2$ images. By $t = 2$ the inner most field line has dissipated. It is quite pleasing, however, to note that the CTU + CT algorithm preserves the circular shape of the magnetic field lines, even at this low resolution.

5.2. Circularly polarized Alfvén wave

The test problem involving the propagation of circularly polarized Alfvén waves at an oblique angle to the grid was described in Section 3.3.2. In this subsection, we present a resolution study for both standing and traveling Alfvén waves. The initial conditions are equivalent to those used in Section 3.3.2 only with $N = \{4,8,16,32\}$.

As a diagnostic of the solution accuracy, we plot the in-plane component of the magnetic field, B_2, perpendicular to the wave propagation direction, x_1, in Fig. 9. These plots are constructed using the cell center components of the magnetic field and each grid cell is included in the plots. Hence, the lack of scatter demonstrates that the solutions retain their planar symmetry quite well. Fig. 9 includes the solutions at time
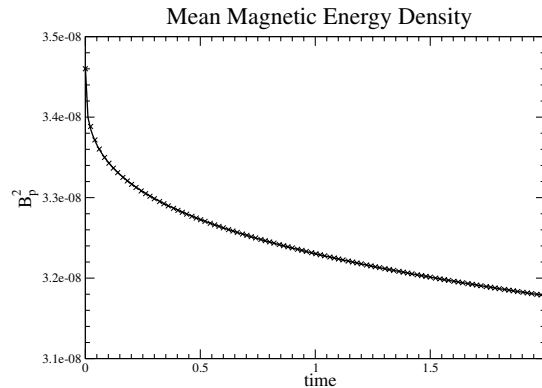

Fig. 7. Plot of the volume averaged magnetic energy density B^2 as a function of time. The solid line is a power law curve fit to the data points denoted by the symbols.
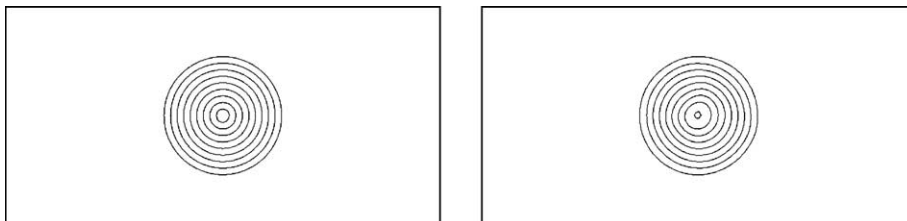

Fig. 8. Magnetic field lines at $t = 0$ (left) and $t = 2$ (right) using the CTU + CT integration algorithm.
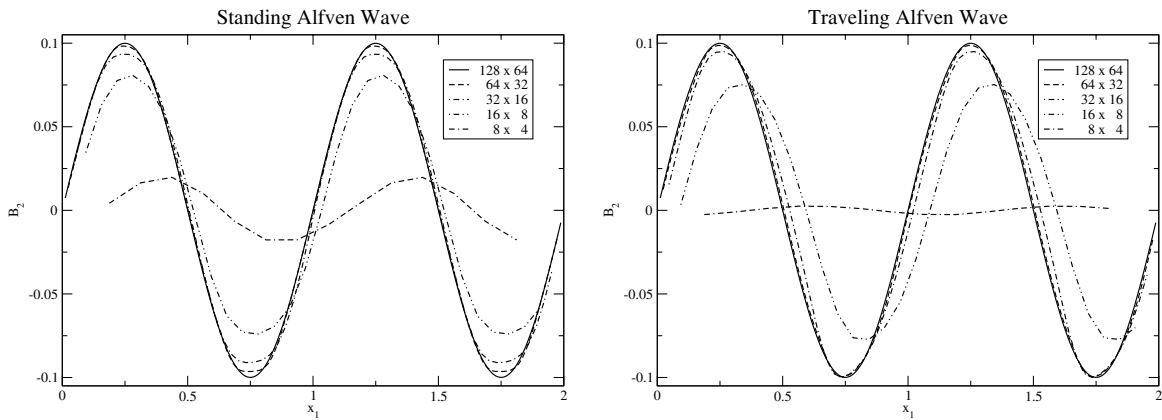
Fig. 9. Plot of B_2 versus x_1 at $t = 5$ for the standing (left) and traveling (right) circularly polarized Alfvén wave problem. For comparison, the initial conditions at $t = 0$ for the $N = 64$ case is also included.

$t = 5$ with $N = \{4, 8, 16, 32\}$ for both standing and traveling waves. For comparison, we also include the initial conditions for the $N = 64$ case. We find that these results compare well against other published calculations [25,32] and we find no indication of the parametric instability for the parameters adopted here.

5.3. Rotated shock tube problem

The solution to the one-dimensional Riemann problem has long been used as a test of numerical algorithms [30,21]. Solving the same problem in a two-dimensional domain with the initially planar discontinuity rotated by some angle with respect the the grid can also be a robust test of the integration algorithm. In addition to the usual questions, one is also interested in how well the planar symmetry is preserved for flows which are oblique to the grid.

For MHD this implies a particularly stringent condition on the component of the magnetic field in the direction of the initial discontinuity normal. Using the coordinate transformations in Eqs. (53)–(55), let the initial discontinuity lie in the plane $x1 = $ constant. Then for MHD, the solution to the one-dimensional Riemann problem should have $B_1 = $ constant, which requires a balance between the x- and y-gradients of $\mathcal{E}_z$ such that $\partial \mathcal{E}_z / \partial x_2 = 0$. Tóth [32] has recently shown that in some cases, schemes which do not preserve the $\nabla \cdot \mathbf{B} = 0$ condition can result in a solution in which B_1 contains a jump across a shock; see also [16].

In the trivial case, rotated shock tube problems are initialized with the shock tube discontinuity oriented at a 45 degree angle with respect to the grid, i.e. with a coordinate rotation angle $\theta = \tan^{-1}(\delta x / \delta y)$. Examples of test calculations performed using this configuration can be found in [11,16,28]. We have run a variety of shock tube problems with this configuration (with both $\delta x = \delta y$ and $\delta x \neq \delta y$) and find that in all of our tests, the parallel component of the magnetic field, B_1, remains equal to a constant with variations which are of the order of roundoff error. We assert that this is a result of the symmetry of the initial conditions with respect to the grid.

A non-trivial configuration with a coordinate rotation angle of $\theta = \tan^{-1}(2) \approx 63.4°$ and $\delta x = \delta y$ was recently suggested by Tóth [32] and has been adopted elsewhere [9,23] as well. This problem is more challenging because at the discrete, grid-scale level the initial conditions contain variations along the plane of the initial shock tube discontinuity. Moreover, the symmetry in this configuration is such that $q_{i,j} = q_{i+2,j-1}$ which is outside of the integration stencil for most integration algorithms. This is especially true in the neighborhood of shocks where most integration algorithms drop to first order. Typically, it is in the neighborhood of shocks where one find oscillations, or in some cases even jumps, in B_1.

We choose to simulate rotated shock tube problems on a grid of $N_x \times N_y$ grid cells with $\delta x = \delta y$ and the shock tube discontinuity oriented along the grid diagonal. Let C equal the greatest common divisor of (N_x, N_y) and define $r_x \equiv N_x/C$ and $r_y \equiv N_y/C$. With this configuration, the coordinate rotation angle $\theta = \tan^{-1}(r^x/r^y)$ and the symmetry is such that $q_{i,j} = q_{i+r_x, j-r_y}$. Note that this computational grid can also be described as containing $C \times C$ "macro-cells" each of which is $r_x \times r_y$ grid cells in size. We have run a variety of shock tube problems with $(r_x, r_y) = (2,1), (3,2), (5,4)$, etc. and in all cases find results which are mutually consistent.

In the interest of presenting solutions which can be compared to previously published results [9,23,32] we will now focus on the $(r_x, r_y) = (2,1)$ case with $N_x = 256$ and $N_y = 128$. The particular problem studied has a left state given by $V^L = (1, 10, 0, 0, 5/\sqrt{4\pi}, 5/\sqrt{4\pi}, 0, 20)$ and a right state given by $V^R = (1, -10, 0, 0, 5/\sqrt{4\pi}, 5/\sqrt{4\pi}, 0, 1)$ where $V = (\rho, v_1, v_2, v_3, B_1, B_2, B_3, P)$. Among other places, the one-dimensional solution to this Riemann problem can be found in Fig. 1a of [27].

In Fig. 10, we present line plots of the parallel component of the magnetic field B_1 versus the parallel coordinate x_1. These line plots include every point in the computational domain, hence the lack of scatter indicates that the solution retains the planar structure quite well. The first line plot, labeled "grid cell", is constructed using the cell center magnetic field components. We find oscillations in B_1 which are roughly 10% of B_1, with the largest oscillations occurring at the fast-mode shocks and weaker oscillations at the left and right propagating slow-mode rarefaction and shock, respectively. We note that the $\mathcal{E}_z^\alpha$ CT algorithm does not reduce these oscillations further when compared to the $\mathcal{E}_z^\circ$ CT algorithm. Hence the oscillations in B_1 are not a result of insufficient dissipation in the CT algorithm. The second line plot, labeled "macro-cell", is constructed by first conservatively averaging the solution onto a grid of 128×128 "macro-cells" before computing the macro-cell center component of B_1. The variations in B_1 when averaged onto a macro-cell are of the order of roundoff error. Note that we obtain the same result for other rotation angles, e.g. with $(r_x, r_y) = (3,2), (5,4)$, etc. We conclude that the oscillations in B_1 versus x_1 are a simple consequence of the fact that on the scale of grid cells, the discretized solution contains variations in the x_2-direction. Upon averaging the solution onto the macro-cells, this variation is eliminated, and we recover the condition $B_1 = $ a constant. Note that this also suggests that if one wishes to eliminate the
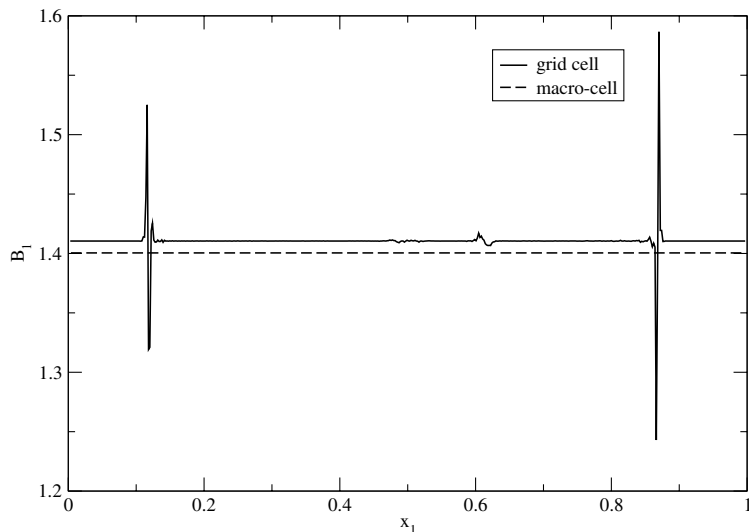

Fig. 10. Plot of B_1 versus x_1 for the $(r_x, r_y) = (2,1)$ case at time $t = 0.08$ using the grid cell centered **B** and the macro-cell centered **B**. The data for the macro-cell centered **B** have been offset vertically by 0.01 to for clarity.

oscillations in B_1 it would require a viscosity with a stencil whose size is at least as large as the macro-cell.

The recovery of B_1 = a constant upon averaging the solution onto a grid of macro-cells is clearly consistent with magnetic flux conservation and plane parallel symmetry, yet it does not appear to be a trivial result. For example, it is clear that schemes which generate a jump in B_1 [16,32] cannot recover this result.

5.4. Linear wave convergence

In this subsection, we show that the CTU + CT integration algorithm converges with second order accuracy for linear amplitude waves. The computational domain extends from $0 \leqslant x \leqslant 2/\sqrt{5}$, and $0 \leqslant y \leqslant 1/\sqrt{5}$, is resolved on a $2N \times N$ grid and has periodic boundary conditions on both x- and y-boundaries. The linear wave propagates at an angle $\theta = \tan^{-1}(2) \approx 63.4°$ with respect to the x-axis and has a wavelength $\lambda = 2/5$. Using the coordinate rotation described by Eqs. (53)–(55), the initial conserved variable state vector is given by

$$q^0 = \bar{q} + \varepsilon R_k \cos(2\pi x_1), \tag{78}$$

where $\bar{q}$ is the mean background state, $\varepsilon = 10^{-6}$ is the wave amplitude, and R_k is the right eigenvector in conserved variables for wave mode k (calculated in the state $\bar{q}$). In order to enable others to perform the same tests presented here and compare the results in a quantitative manner, we include the numerical values for the right eigenvectors in Appendix A. As in previous 2D calculations, the in-plane components of the magnetic field (B_x, B_y) are initialized via the z-component of the magnetic vector potential.

The mean background state $\bar{q}$ is selected so that the wave speeds are well separated and there are no inherent symmetries in the magnetic field orientation. It is most convenient to describe it in terms of the associated primitive variables and in the rotated coordinate system given by Eqs. (53)–(55). The density $\bar{\rho} = 1$ and gas pressure $\bar{P} = 1/\gamma = 3/5$. The velocity component parallel to the wave propagation direction, $\bar{v}_1 = 1$ for the entropy mode test and $\bar{v}_1 = 0$ for all other wave modes. The transverse velocity components $\bar{v}_2 = \bar{v}_3 = 0$. The magnetic field components $\bar{B}_1 = 1$, $\bar{B}_2 = \sqrt{2}$, and $\bar{B}_3 = 1/2$. With this choice, the slow mode speed $c_s = 1/2$, the Alfvén speed $c_a = 1$, and the fast mode speed $c_f = 2$ in the wave propagation direction.

The error in the solution is calculated after propagating the wave for a distance equal to 1 wavelength. Hence, the initial state is evolved for a time $t = \lambda/c$ where c is the speed of the wave mode under consideration. For each component k of the conserved variable vector q we calculate the L1 error with respect to the initial conditions

$$\delta q_k = \frac{1}{2N^2} \sum_i \sum_j |q_{i,j,k}^n - q_{i,j,k}^0| \tag{79}$$

by summing over all grid cells (i,j). We use the cell center components of the in-plane magnetic field components (B_x, B_y) in computing this error. In Fig. 11, we plot the norm of this error vector

$$|\delta q| = \sqrt{\sum_k (\delta q_k)^2} \tag{80}$$

for the fast, Alfvén, slow and entropy modes. This plot shows that the solution for each wave mode converges with at least second order accuracy. The order of convergence for each wave mode, obtained by a power law fit to the errors, is indicated in the legend of Fig. 11. We note in passing that if the interface state reconstruction algorithm is performed using piecewise linear interpolation, instead of piecewise quadratic, the error is proportional to N^{-2} for all wave modes and the amplitude is increased slightly.
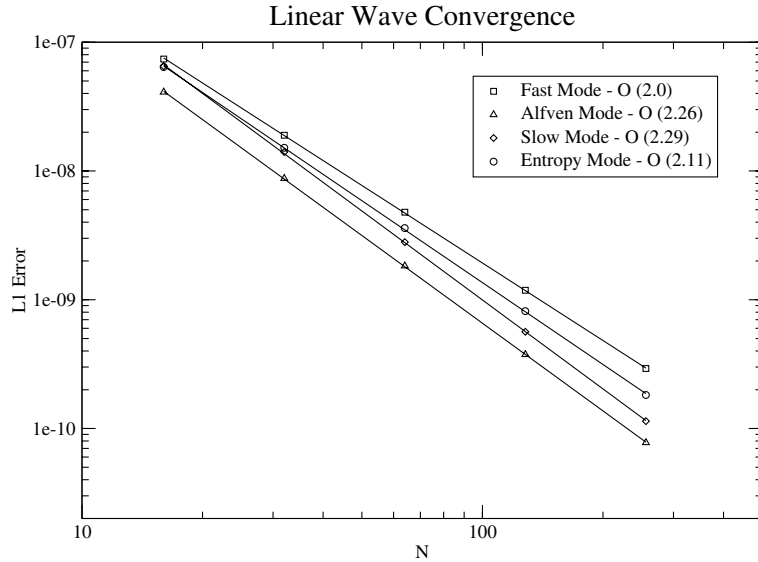
Linear Wave Convergence

Fig. 11. Linear wave convergence of fast, Alfvén, slow and entropy modes using the CTU + CT integration algorithm. The symbols denote the calculated L1 error norm. The lines are power law curve fits to the data and the order of convergence for each wave mode is indicated in the legend.

5.5. Current sheet

In this subsection, we present a problem which is particularly sensitive to the numerical dissipation and demonstrates of the robustness of the integration algorithm. The computational domain extends from $0 \leqslant x \leqslant 2$, and $0 \leqslant y \leqslant 2$, is resolved on an 256×256 grid and has periodic boundary conditions on both x- and y-boundaries. The density $\rho = 1$ and the magnetic field components $B_x = B_z = 0$ and

$$
B_y = \begin{cases} B_0 & \text{if } 0 \leqslant x < 1/2, \\ -B_0 & \text{if } 1/2 \leqslant x \leqslant 3/2, \\ B_0 & \text{if } 3/2 < x \leqslant 2, \end{cases} \tag{81}
$$

where $B_0 = 1$. Hence there are initially two current sheets in the computational domain and the characteristic Alfvén speed $c_a = B_0/\sqrt{\rho} = 1$. The gas pressure $P = 0.1$ such that $\beta = 2P/B_0^2 = 0.2$ and the dynamics are initially magnetically dominated. The ratio of the Alfvén speed to the sound speed $B_0/\sqrt{\gamma P} \approx 2.45$, hence magnetically driven dynamics are supersonic. The initial velocity components $v_x = v_0 \sin(\pi y)$ with $v_0 = 0.1$, $v_y = v_z = 0$. For $v_0/c_a \ll 1$ the ensuing dynamics are well characterized by linear Alfvén waves. For the values selected here this is approximately true at early times, until magnetic reconnection and nonlinear effects come to influence the dynamics.

One aspect of this problem which is of particular interest is the magnetic reconnection since it is a direct measure of the numerical resistivity. In Fig. 12, we present the time evolution of the magnetic field lines. From the magnetic field geometry at time $t = 0.5$ we see that, as one should expect, the numerical resistivity is a function of the magnetic field orientation with respect to the grid: magnetic fields dissipate, and reconnect preferentially where the magnetic field orientation is oblique to the grid. Hence, we find the largest change in the magnetic field structure at the nodal points of the transverse velocity. As reconnection takes place, the magnetic energy is converted into thermal energy (on time scales of the integration time step) which in turn drives both compressional, and Alfvénic waves. These waves interact seeding more reconnection events. By time $t = 1$ a series of magnetic islands have developed along the current sheets. These islands are free to move parallel to
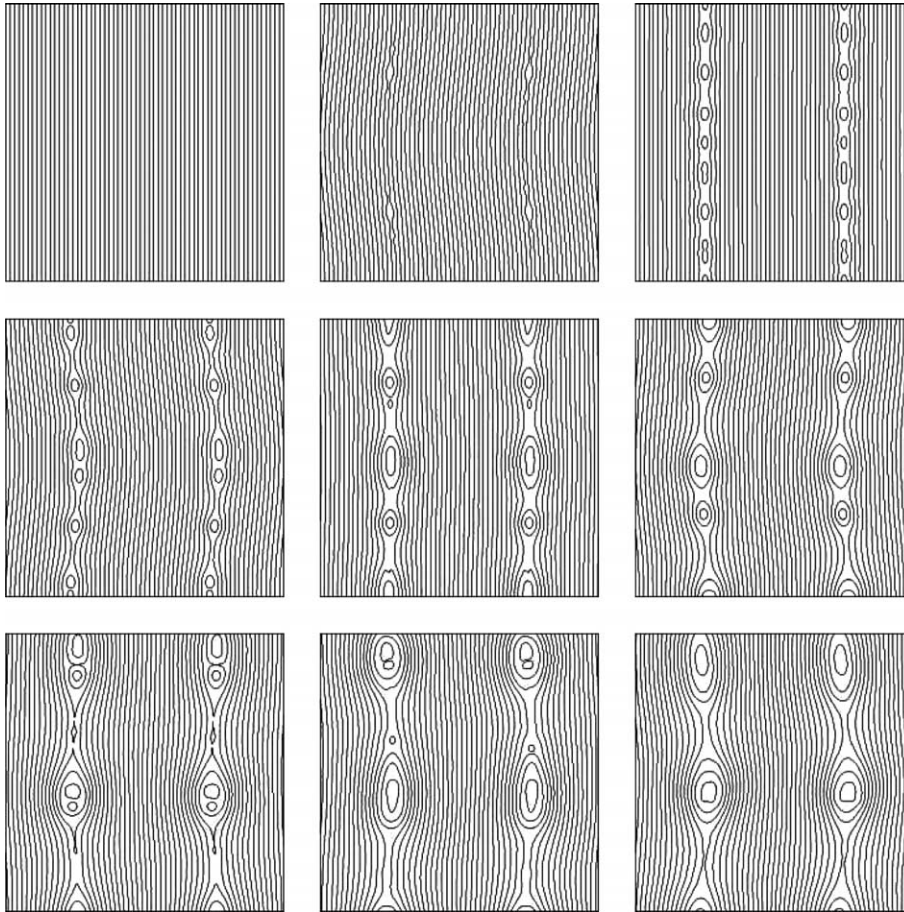
Fig. 12. Time evolution of the magnetic field lines using the CTU + CT integration algorithm. Time increases from left to right and top to bottom in normal reading order. The contour levels of A_z which are plotted is uniform over the sequence of images at times $t = (0,0.5,1.0,1.5,2.0,2.5,3.0,3.5,4.0)$.

the local magnetic field direction and by time $t = 1.5$ some of the magnetic islands have propagated toward the velocity anti-nodes and merged. This process of island formation, translation, and merging continues until there are two magnetic field islands along each current sheet located approximately at the velocity anti-nodes.

This problem is also interesting in that it uses a very simple set of initial conditions to test the "robust-ness" of the integration algorithm. The nonlinear dynamics which result from this problem lead to strong compressions and rarefactions. It is important to maintain the divergence-free constraint as the topology of the field changes during reconnection. By either increasing v_0 or decreasing P (and therefore β) the dynam-ics become increasingly difficult for the integration algorithm to solve. We have found it a very useful test to discriminate between algorithms.

5.6. MHD blast wave

As our final test problem we consider the explosion of a centrally over pressurized region into a low pres-sure, low β ambient medium. This problem has been studied by a number of authors [3,22,33] and we have chosen to use the parameters given by [22]. The computational domain extends from $-0.5 \leqslant x \leqslant 0.5$ and
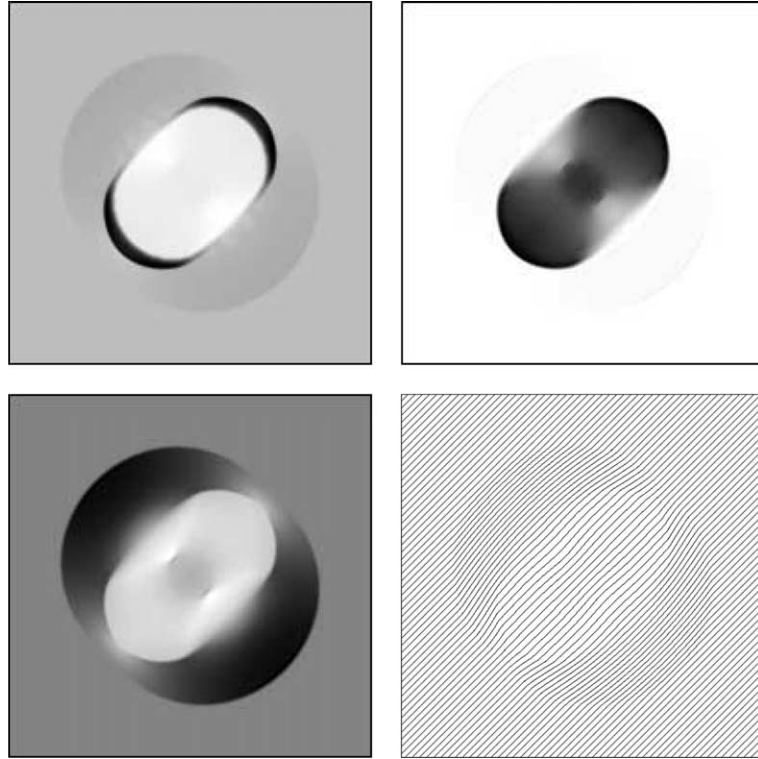
Fig. 13. Linearly scaled gray-scale images and the magnetic field lines of the evolved state (time = 0.2) for the MHD blast wave problem. The density (top left) ranges from 0.192 (white) to 3.31 (black). The gas pressure (top right) ranges from 1.0 (white) to 32.1 (black). The magnetic energy density (bottom left) ranges from 23.5 (white) to 77.7 (black).

$-0.5 \leqslant y \leqslant 0.5$. The density $\rho = 1$, the velocity $\mathbf{v} = 0$, and the magnetic field components $B_x = B_y = 10/\sqrt{2}$ and $B_z = 0$. Within a circle of radius $R = 0.125$ about the origin the gas pressure $P = 100$ and $\beta = 2P/B^2 = 2$. Outside of this circle, the gas pressure $P = 1$ and $\beta = 2 \times 10^{-2}$.

The solution to this problem at time $t = 0.2$, using a 200×200 grid, is presented in Fig. 13. The density image shows two dense shells of gas which propagate parallel to the magnetic field. The outer surface of these shells is a slow-mode shock and the inner surface is the contact surface separating the gas initially inside and outside of the boundary surface. The maximum compression of the gas is 3.3 indicating that the slow mode shock is quite strong, in agreement with what one might expect from the ratio of the gas pressures, $P_{in}/P_{amb} = 100$. In the direction orthogonal to the magnetic field, the magnetic pressure is the dominant player in the dynamics, yet from the field lines we see that there is only a moderate change in the geometry of the field.

The solution presented in Fig. 13 demonstrates that the algorithm presented in this paper is both stable and accurate for low-β plasma problems involving strong MHD shock waves. The solutions also preserve the initial symmetry of the flow exceptionally well despite the orientation of the magnetic field. We find no indication of grid related artifacts in the solution.

6. Conclusion

In this paper, we have demonstrated that the method of constrained transport can be combined with finite volume integration algorithms in a self consistent manner. Consistency, however, implies that the

electric fields used in the CT update step and those used for evolving the volume average magnetic fields are coupled. This coupling has direct consequences for the stability and accuracy of the integration algorithm. We have presented a general approach to constructing CT algorithms, constructing and testing three. Each of these CT algorithms contained the novel property that for planar, grid-aligned flows the solution would recover the 1D solution obtained with the underlying integration algorithm. These CT algorithms differed only in their dissipation properties for truly multidimensional flows. Through numerical experiments we have shown that the $\mathscr{E}_z^c$ CT algorithm is well behaved leading to stable, non-oscillatory solutions. We have also noted how this algorithm can readily be combined with other unsplit integration algorithms such as central schemes, or wave propagation methods.

We have shown that if the PPM integration algorithm is used for ideal MHD, terms proportional to $\partial B_x/\partial x$ and $\partial B_y/\partial y$, which in primitive variables are present only in the induction equation, must be included in the calculation of the "interface states". If these terms are neglected in the calculation of the interface states, the integration algorithm is oscillatory for the simple case of field loop advection. We also presented two simple *gedanken* experiments to demonstrate why this result should be expected. A simple approach for including these source terms in the calculation of the interface states is adopted and it has been demonstrated to be accurate and stable for use with both the single step and two step (CTU + CT) integration algorithm.

Another result of this paper is the extension of the CTU integration algorithm for ideal MHD based upon the CT integration algorithm. We showed that since the interface states are calculated using primitive variables, the standard CTU procedure for updating the interface states to the 1/2 time step is missing terms which are proportional to $\partial B_x/\partial x$ at x-interfaces and similarly for the y-interface states. These terms must be included as an additional set of "source terms" so that the interface states are formally advanced to the 1/2 time step. We also described how the CT algorithms developed in this paper can be combined with the CTU integration algorithm so as to maintain $\nabla \cdot \mathbf{B} = 0$ throughout the integration time step.

The CTU + CT integration algorithm presented in this paper for ideal MHD has been thoroughly tested and some representative solutions have been included here. This algorithm combines the strong stability and shock capturing characteristics of Godunov methods with the magnetic flux conservation obtained via the CT method. The integration algorithm is conservative, uses a single step update algorithm, and is second order accurate on smooth solutions. These characteristics make it ideally suited for use on either a statically or adaptively refined mesh. We note also that "physical" source terms such as an external gravitational field, or Coriolis terms accounting for a rotating reference frame can be readily incorporated into this integration algorithm. The resulting algorithm also retains the desirable properties noted above, such as recovering the 1D solution for plane parallel grid-aligned flows. These details will be described in a later paper.

Lastly, while the algorithm presented in this paper has focused solely on the two-dimensional case, the results presented here can be extended to three dimensions. This extension principally involves modifications to the "source terms" involved in the calculation and update of the interface states with transverse flux gradients. The actual details of this extension are beyond the scope of this paper and will be presented elsewhere.

Appendix A. Linear wave right eigenvectors

In order to enable others to perform the linear wave convergence test presented in Section 5.4 and compare their results in a quantitative manner, we include the numerical values for the right eigenvectors here. In the rotated coordinate system described by Eqs. (53)–(55) the conserved variable vector

$$q = \begin{pmatrix} \rho \\ \rho v_1 \\ \rho v_2 \\ \rho v_3 \\ B_1 \\ B_2 \\ B_3 \\ E \end{pmatrix}. \tag{A.1}$$

The right eigenvectors (labeled according to their propagation velocity) are given by

$$R_{\pm c_f} = \frac{1}{6\sqrt{5}} \begin{pmatrix} 6 \\ \pm 12 \\ \mp 4\sqrt{2} \\ \mp 2 \\ 0 \\ 8\sqrt{2} \\ 4 \\ 27 \end{pmatrix}, \quad R_{\pm c_a} = \frac{1}{3} \begin{pmatrix} 0 \\ 0 \\ \pm 1 \\ \mp 2\sqrt{2} \\ 0 \\ -1 \\ 2\sqrt{2} \\ 0 \end{pmatrix}, \tag{A.2}$$

$$R_{\pm c_s} = \frac{1}{6\sqrt{5}} \begin{pmatrix} 12 \\ \pm 6 \\ \pm 8\sqrt{2} \\ \pm 4 \\ 0 \\ -4\sqrt{2} \\ -2 \\ 9 \end{pmatrix}, \quad R_{v_1} = \frac{1}{2} \begin{pmatrix} 2 \\ 2 \\ 0 \\ 0 \\ 0 \\ 0 \\ 0 \\ 1 \end{pmatrix}. \tag{A.3}$$

References

[1] D.S. Balsara, Second order accurate schemes for magnetohydrodynamics with divergence-free reconstruction, astro-ph/0308249.
[2] D.S. Balsara, J. Kim, An Intercomparison between divergence-cleaning and staggered mesh formulations for numerical magnetohydrodynamics, astro-ph/0310728.
[3] D.S. Balsara, D.S. Spicer, A staggered mesh algorithm using high order Godunov fluxes to ensure solenoidal magnetic fields in magnetohydrodynamic simulations, J. Comput. Phys. 149 (1999) 270.
[4] J.U. Brackbill, D.C. Barnes, The effect of nonzero $\nabla \cdot \mathbf{B}$ on the numerical solution of the magnetohydrodynamic equations, J. Comput. Phys. 35 (1980) 426.

  [5] P. Cargo, G. Gallice, Roe matrices for ideal MHD and systematic construction of Roe matrices for systems of conservation laws, J. Comput. Phys. 136 (1997) 446.

  [6] D.A. Clarke, A consistent method of characteristics for multidimensional magnetohydrodynamics, Astrophys. J. 457 (1996) 291.

  [7] P. Colella, Multidimensional upwind methods for hyperbolic conservation laws, J. Comput. Phys. 87 (1990) 171.

  [8] P. Colella, P.R. Woodward, The piecewise parabolic method (PPM) for gas-dynamical simulations, J. Comput. Phys. 54 (1984) 174.

  [9] R.K. Crockett, P. Colella, R.T. Fisher, R.I. Klein, C.F. McKee, An unsplit, cell-centered Godunov method for ideal MHD, J. Comput. Phys. 203 (2005) 422.

[10] W. Dai, P.R. Woodward, A high-order Godunov-type scheme for shock interactions in ideal magnetohydrodynamics, SIAM J. Sci. Comput. 18 (4) (1997) 957.

[11] W. Dai, P.R. Woodward, A simple finite difference scheme for multidimensional magnetohydrodynamical equations, J. Comput. Phys. 142 (1998) 331.

[12] A. Dedner, F. Kemm, D. Kröner, C.-D. Munz, T. Schnitzer, M. Wesenberg, Hyperbolic divergence cleaning for the MHD equations, J. Comput. Phys. 175 (2002) 645.

[13] L. Del Zanna, M. Velli, P. Londrillo, Parametric decay of circularly polarized Alfvén waves: multidimensional simulations in periodic and open domains, Astron. Astrophys. 367 (2001) 705.

[14] B. Einfeldt, On Godunov-type methods for gas dynamics, SIAM J. Numer. Anal. 25 (2) (1988) 294.

[15] C.R. Evans, J.F. Hawley, Simulation of magnetohydrodynamic flows: a constrained transport method, Astrophys. J. 322 (1988) 659.

[16] S.A.E.G. Falle, S.S. Komissarov, P. Joarder, A multidimensional upwind scheme for magnetohydrodynamics, Month. Notices R. Astron. Soc. 297 (1998) 265.

[17] M.L. Goldstein, An instability of finite amplitude circularly polarized Alfvén waves, Astrophys. J. 219 (1978) 700.

[18] A. Harten, P.D. Lax, B. Van Leer, On upstream differencing and Godunov-type schemes for hyperbolic conservation laws, SIAM Rev. 25 (1) (1983) 35.

[19] J.O. Langseth, R.J. LeVeque, A wave propagation method for three-dimensional hyperbolic conservation laws, J. Comput. Phys. 165 (2000) 126.

[20] S. Li, HLLC Riemann solver for magnetohydrodynamics, J. Comput. Phys. 203 (2005) 344.

[21] R. Liska, B. Wendroff, Comparison of several difference schemes on 1D and 2D test problems for the Euler equations, SIAM J. Sci. Comput. 25 (3) (2003) 995.

[22] P. Londrillo, L. Del Zanna, High-order upwind schemes for multidimensional magnetohydrodynamics, Astrophys. J. 530 (2000) 508.

[23] P. Londrillo, L. Del Zanna, On the divergence free condition in Godunov-type schemes for ideal magnetohydrodynamics: the upwind constrained transport algorithm, J. Comput. Phys. 195 (2004) 17.

[24] G.H. Miller, P. Colella, A conservative three-dimensional Eulerian method for coupled solid-fluid shock capturing, J. Comput. Phys. 183 (2002) 26.

[25] U. Pen, P. Arras, S. Wong, A free, fast, simple and efficient TVD MHD code, Astrophys. J. Suppl. 149 (2003) 447.

[26] K.G. Powell, P.L. Roe, T.J. Linde, T.I. Gombosi, D.L. De Zeeuw, A solution-adaptive upwind scheme for ideal magnetohydrodynamics, J. Comput. Phys. 154 (1999) 284.

[27] D. Ryu, T.W. Jones, Numerical magnetohydrodynamics in astrophysics: algorithm and tests for one-dimensional flow, Astrophys. J. 442 (1995) 228.

[28] D. Ryu, F. Miniati, T.W. Jones, A. Frank, A divergence-free upwind code for multidimensional magnetohydrodynamic flows, Astrophys. J. 509 (1998) 244.

[29] J. Saltzman, An unsplit 3D upwind method for hyperbolic conservation laws, J. Comput. Phys. 115 (1994) 153.

[30] G.A. Sod, A survey of several finite difference schemes for hyperbolic conservation laws, J. Comput. Phys. 27 (1978) 1.

[31] J.M. Stone, M.L. Norman, ZEUS-2D: a radiation magnetohydrodynamics code for astrophysical flows in two space dimensions. II. The magnetohydrodynamic algorithms and tests, Astrophys. J. Suppl. 80 (1992) 791.

[32] G. Tóth, The $\nabla \cdot \mathbf{B} = 0$ constraint in shock-capturing magnetohydrodynamics codes, J. Comput. Phys. 161 (2000) 605.

[33] A.L. Zachary, A. Malagoli, P. Colella, A higher-order Godunov method for multidimensional ideal magnetohydrodynamics, SIAM J. Sci. Comput. 15 (1994) 263.